3464 *Chem. Mater.* **2001,** *13,* 3464−3486

Block Copolymer−Ceramic Hybrid Materials from Organically Modified Ceramic Precursors

Peter F. W. Simon,[†] Ralph Ulrich,[‡,§] Hans W. Spiess,[‡] and Ulrich Wiesner*,[†]

Department of Materials Science and Engineering, Cornell University, 329 Bard Hall,
Ithaca, New York 14853, and Max-Planck-Institute for Polymer Research, Ackermannweg 10,
55128 Mainz, Germany

Received February 23, 2001. Revised Manuscript Received May 22, 2001

The study of amphiphilic polymer based functional organic−inorganic hybrid materials is an emerging research area offering enormous scientific and technological promise. Here, we show that employing poly(isoprene-*block*-ethylene oxide) block copolymers (PI-*b*-PEO) and a silicon precursor, which contains a polymerizable organic moiety, unprecedented morphology control on the nanoscale is obtained. This control is based on a unique polymer−ceramic interface, which is characterized using a multi-nuclei solid-state NMR approach. The results show that the hydrophilic parts of the polymer are completely integrated into the ceramic phase, thereby leading to a quasi "two-phase system", allowing for a more rational hybrid morphology design based on the current understanding of the phase behavior of block copolymers and copolymer−homopolymer mixtures. Examination of the full phase space of the hybrid materials reveals the existence of a new bicontinuous cubic structure that was not known to exist in polymer systems. SAXS and TEM data of this structure are consistent with a so-called "Plumber's nightmare" morphology. Selective solvent swelling of the hydrophobic parts of the hybrids leads to isolated nano-objects of different shapes, sizes, and compositions, while heat treatment generates mesoporous ceramic materials in which the mesostructure of the precursor material is preserved. Potential applications of these materials ranging from nanobiotechnology to catalysis are discussed.

1. Introduction

Control of the shape and size of organic−inorganic hybrid materials is a key feature of natural growth phenomena. Both are a result of long evolutionary optimization processes and are intimately related to specific functions.[1] In biomineralization, complex architectures on different length scales are usually obtained through cooperative self-assembly of organic and inorganic species.[2−4] Despite the success in understanding the basic principles of self-assembly,[5−8] it remains a challenge for scientists to mimic such natural pathways and develop simple but efficient routes to materials structured all the way down to the nanometer scale.[9−17]

Since all biological systems are based on water as the solvent, the role of organic amphiphiles in structure formation processes is of key interest. The self-assembly of small amphiphilic molecules in an aqueous solution was first investigated by Luzzati et al.[18,19] They discovered that biological amphiphiles can form ordered structures on the nanometer scale. From then on a range of bilayer aggregates of small amphiphilic molecules such as flat sheets (lamellae), closed spherical aggregates (vesicles or liposomes), and tubules has been found and explored extensively. This forms the basis of intense research activities now moving toward potential applications as complex as drug delivery.[20−25]

Block copolymers can be regarded as macromolecular analogs of low molecular weight surfactants.[26−30] Their self-assembly in block-selective solvents has been shown to result in a variety of nanoscale morphologies including spheres, rods, lamellae, vesicle tubules, cylinders, and large compound vesicles, micelles, or rod micelles.[31−41] In particular, crew-cut micelle-like aggregates[42] of various morphologies have been obtained by aqueous solutions of amphiphilic diblock copolymers and their conformational characteristics are extensively discussed in the literature.[36,43−49] Moving from solution to condensed phases, the self-assembly of block copolymers in bulk has also attracted much research interest.[8] The phase behavior was found to be similar to low molecular weight nonionic surfactants[26] and numerous experimental as well as theoretical studies have helped to elucidate specific phase diagrams.[50]

The use of self-assembly to gain structured organic−inorganic composites on the nanometer scale is appealing since no special machining, other than combining the "right" components under the "right" conditions is required. Block copolymer self-assembly is particularly interesting. As in the case of unstructured hybrids, the best features of inorganic oxides and organic polymers are combined (cf. the use in contact lenses, waveguides, scratch-resistant coatings, data-storage devices, chemical filters, biosensors, electrolytes, and dental fillings[51,52]). At the same time block copolymers allow control of organic−inorganic hybrid morphology down to the nanometer scale. Since macroscopic property profiles crucially depend on both composition *and*

---

* To whom correspondence should be addressed. E-mail: ubw1@cornell.edu.
[†] Cornell University.
[‡] Max-Planck-Institute for Polymer Research.
[§] Present address: Bayer AG, Plastics Division, Rheinuferstrasse 7-9, Building R33, 47892 Krefeld, Germany.

10.1021/cm0110674 CCC: $20.00

morphology, properties can thus be tailored over a wide range.

The present review article will focus on a particular class of block copolymer−ceramic hybrid materials in which the inorganic precursor itself gives rise to an organically modified ceramic (ormocer) material. In particular, the structure-directing properties of an amphiphilic poly(isoprene-*block*-ethylene oxide) block copolymer (PI-*b*-PEO) during the sol−gel synthesis of an organically modified aluminosilicate network based on 3-(gycidyloxypropyl)trimethoxysilane, GLYMO, and aluminum *sec*-butoxide, $Al(O^sBu)_3$, will be described.[53,54]

The article is organized as follows: In the first part, properties of both inorganic and organic components will be highlighted individually. Structural aspects of the sol−gel network and the phase behavior of the block copolymer will be discussed. In the second part, the structure-directing effects of the polymer on the inorganic network will be outlined, employing results of small-angle X-ray scattering (SAXS) and transmission electron microscopy (TEM). To gain a deeper understanding of the guiding principles in the structural control, the hybrid interface will be examined in more detail using solid-state NMR techniques. In the proceeding part, the full phase space of block copolymers will be explored in the hybrid material synthesis. A new bicontinuous cubic morphology will be described, which to the best of our knowledge was not known for polymers. Finally, use of these nanostructured hybrid materials for the preparation of isolated nano-objects with controlled shapes, sizes, and compositions and for the production of mesoporous materials is demonstrated. Potential applications of these materials are discussed in fields ranging from nanobiotechnology to catalysis.

2. Unstructured Organic−Inorganic Hybrid Materials

2.1. Synthesis of Hybrid Materials Using Sol−Gel Chemistry. Organic−inorganic hybrid materials can be obtained through a combination of organic and inorganic components via a sol−gel process. Three different approaches of organic−inorganic hybrid materials are distinguished:[55] (a) impregnation of a porous silicon dioxide matrix by organic components, which can be polymerized in situ, (b) dispersion or solvation of the organic compound in a sol−gel mixture, and (c) use of educts with at least one direct heteroatom−carbon bond.[56−59] As starting materials for the sol−gel process, compounds of different reactivity can be used.[60] Silicon alkoxides need catalysis by an electrophile or a nucleophile,[61] whereas the alkoxides of metals such as titanium, zirconium, or aluminum react without external stimuli.[59] The process as such can be regarded as processing in two steps. In the first step, the inorganic compound is hydrolyzed. This leads to the corresponding hydroxide groups which in the second step react with the remaining unhydrolyzed ones to form a three-dimensional network.[62] During the condensation process, reaction products such as water or alcohol are formed, causing a considerable shrinkage of the material.[63] The general reaction pathway is outlined in Scheme 1 for silicon ethoxide.

The final structure and morphology of the network highly depends on the reaction conditions. Even small variations in temperature, solvent quality, and concentration of the reactants or catalyst may influence the final properties of the resulting gel, like the density and pore size distribution.

Scheme 1. Principal Reactions in the Sol−Gel Process of Silicon Ethoxide

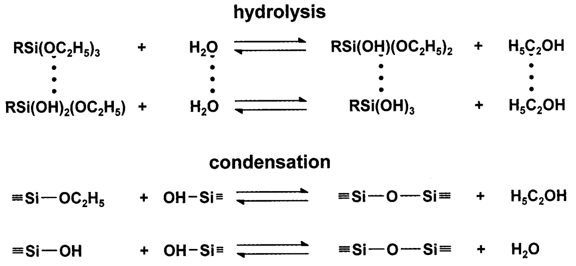

Scheme 2. Schematic Drawing of an Organic−Iorganic Hybrid Material Together with the Nuclei Probed in NMR

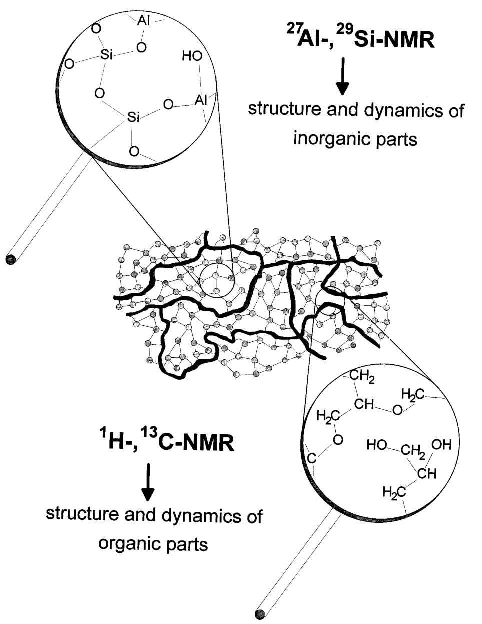

2.2. Characterization of Unstructured Hybrid Materials by Solid-State NMR Techniques. 2.2.1. Information from NMR Spectroscopy. A deeper understanding of the relationship between the macroscopic properties and the structure and dynamics on the microscopic level is crucial for the improvement of hybrid materials. Templin et al.[64] investigated the structural aspects of an aluminosilicate-based hybrid material on the molecular level by multinuclear solid-state NMR.[65−68] They used various advanced NMR techniques under magic-angle spinning conditions (MAS),[67,69] which enabled them to probe the chemical environment of different nuclei and the local dynamics very precisely, as outlined in Scheme 2.

As starting material for the sol−gel process, 3-(glycidyloxypropyl)trimethoxylsilane, GLYMO, an alkoxysilane containing an epoxide ring as a polymerizable group attached to the silicon was used by Templin et al.[64] (cf. Scheme 3). Sols were prepared at 0 °C by mixing GLYMO with aluminum *sec*-butoxide, $Al(O^sBu)_3$, in the presence of diluted hydrochloridic acid. Solidification was achieved by a stepwise temperature increase up to 130 °C within 24 h.

Scheme 3. Possible Ring-Opening Reactions of (3-Glycidyloxypropyl)trimethoxylsilane, GLYMO, in the Presence of Aluminum *sec*-Butoxide, Al(O^{s}Bu)$_3$: (i) Step Polymerization; (ii) Hydrolysis; (iii) Methanolysis

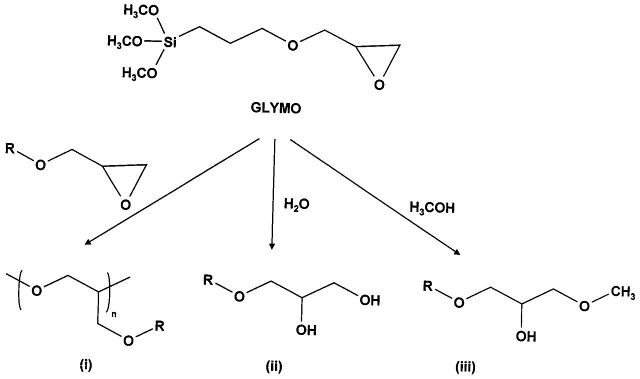

2.2.2. Organic Part. The organic part of the composite material was characterized by solid-state ^{13}C MAS NMR. Representative spectra, recorded with cross polarization (CP),[70] showed that the reactive epoxy ring of GLYMO was stable in the absence of Al(O^{s}Bu)$_3$. The addition of aluminum alkoxide to the sol considerably changed the ^{13}C CP-MAS spectra. Even the addition of only 1 mol % aluminum alkoxide caused the epoxy ring signals to disappear. They concluded that the Al(O^{s}Bu)$_3$ mainly catalyzes the epoxy ring-opening reaction. This result was corroborated very recently by Innocenzi et al.,[71] who obtained similar results using boron trifluoride etherate as the catalyst.

The gelation reaction could follow three possible pathways, which are outlined in Scheme 3. (i) Reaction to oligo- or poly(ethylene oxide) derivatives by step polymerization of the epoxy group, (ii) hydrolysis of the epoxy group yielding a diol, or (iii) formation of a methyl ether by methanolysis.

The reaction products of all pathways were detected in the ^{13}C CP-MAS spectra. Furthermore, single-pulse spectra revealed that at least 25% of the epoxy rings is converted by methanol or water. This leads to the conclusion that oligomers of ethylene oxide are formed rather than a poly(ethylene oxide) with high molecular weight.

2.2.3. Inorganic Part. Information about the inorganic part of the composite material was provided by ^{27}Al and ^{29}Si NMR measurements. For aluminum, chemical shifts have been shown to be sensitive to the coordination number,[72] whereas in ^{29}Si NMR next-nearest-neighbor effects could be probed, respectively.[65,73,74]

Typical results from a single-pulse ^{27}Al MAS NMR for a sample with 10 mol % Al(O^{s}Bu)$_3$ showed tetrahedrally (at 55.2 ppm) and octahedrally (at 5.4 ppm) coordinated aluminum species (cf. Figure 6). The authors concluded that tetrahedrally coordinated aluminum is incorporated into the aluminosilicate lattice[65] while the octahedrally coordinated aluminum is distributed in aluminumoxohydroxo domains $AlO_x(OH)_y(H_2O)_z$.[64]

Further information on the inorganic part can be obtained from ^{29}Si NMR. For the organosilicate species with a direct Si−C bond, the coordination number of the silicon is described by the notation T^n ($n = 0, 1, 2,$ or 3) where n is the number of bridging oxygen atoms (Si−O−Si or Si−O−Al). Different T^n species resonate at a different chemical shift in a ^{29}Si spectrum.[64] A comparison of the ^{29}Si CP-MAS spectra of GLYMO before and after the addition of Al(O^{s}Bu)$_3$ lead to four main differences: (i) the peaks became broader, (ii) the intensity in the area of T^1 and mainly T^2 groups increased, (iii) the maxima of the T^3 and T^2 signals were shifted downfield, and (iv) a new peak at −46.5 ppm arose. The significant broadening observed indicates a broad distribution of environments in the second coordination sphere of silicon as expected for amorphous composites. Moreover, the intensity increase in the chemical shift area of purely siliceous groups is consistent with the appearance of T^3 and T^2 species such as RSi(OAl)$_2$(OSi) or RSi(OAl)$_2$(OH) in the network. The chemical shift of the new peak lies between that of purely siliceous T^0 and T^1 units. Because the spin−lattice relaxation time T_1 (obtained by a single-pulse experiment) is more than 1 order of magnitude larger[75] than what is usually obtained for T groups (20−40 s),[68] this group is probably in a more rigid environment than the other T units. Templin et al.[75] attributed such hindered mobility to silicon units which are localized in pockets of aluminum−oxohydroxo complexes, whereas the observed downfield chemical shift was explained by the presence of three aluminum atoms in the second-coordination sphere around these T^3 groups.[76]

Scheme 4. Structural Model for the GLYMO/Al(O^{s}Bu)$_3$ System

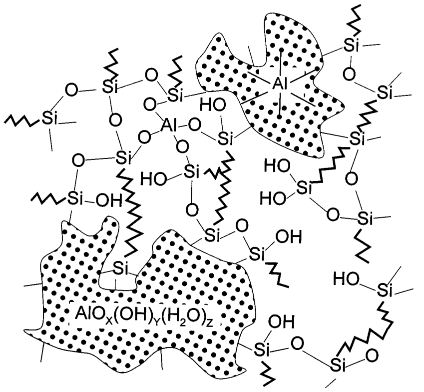

2.3. Structural Model of the Unstructured Organic−Inorganic Hybrid Materials. By combination of the various NMR results, Templin et al.[75] proposed a structural model for the GYMO Al(O^{s}Bu)$_3$ composite, which is shown in Scheme 4.

This model features two different aluminum coordinations (6-fold and 4-fold) and three different surroundings of the silicon in the second coordination sphere (only silicon, only aluminum, or both together). A higher network density is obtained through short links of oligo(ethylene oxide) between different silicon centers.

3. Structured Organic−Inorganic Hybrid Materials

Employing self-assembling organic molecules as structure-directing agents can be regarded as the most promising strategy for preparing ordered hybrid materials. This pathway has already been successfully used in the synthesis of inorganic mesoporous materials.[77,78]

The final morphology is then determined by the cooperative organization of organic and inorganic molecular species into three-dimensional structured arrays—driven by either ionic[11,79−81] or hydrogen bonds[82−84]—a concept also discussed in the context of biomineralization.[10]

Block copolymers as structure-directing agents have been used by different authors: Bagshaw et al.[82] used block-type low molecular weight nonionic surfactants as templating agents to produce mesoporous molecular sieves. Higher molecular weight block copolymers have been used to stabilize inorganic metal or semiconductor nanopartcles[85−91] with morphologies never far from spherical.[14] Very recently, Raez et al.[92] demonstrated the formation of novel organometallic nanotubes by the self-assembly of a poly(ferrocenyldimethylsilane-*b*-dimethylsiloxane) block copolymer. In this elegant approach organometallic segments are combined with organic or inorganic blocks, which offers the opportunity to access self-assembled materials with redox-active, semiconducting, or preceramic nanodomains.[93−97] The transition from the small to the large mesoscopic regime of silica-type mesostructures was achieved by Templin et al.[53] using a poly(isoprene-*b*-ethylene oxide), PI-*b*-PEO, block copolymer of higher molecular weight; see below.

3.1. Phase Behavior and Phase Transition of Poly(isoprene-*b*-ethylene oxide). The phase behavior of block copolymers can be described theoretically by different approaches.[50,98] According to the mean-field theory (MFT),[99] the block copolymer phase behavior is dictated by the Flory−Huggins segment−segment interaction parameter, χ, the degree of polymerization, N, and the composition, f, with the product $N\chi$ determining the degree of segregation. In the case $N\chi \leq 10$, the system is ruled by entropic terms, resulting in a disordered phase. Under the condition $N\chi > 10$, enthalpic terms dominate, causing an order-to-disorder transition, ODT, where the unlike segments segregate into a variety of ordered periodic microstructures. For nearly symmetric compositions the unlike blocks form domains composed of alternating layers, known as lamellar phase (*lam*). Slightly off-symmetry results in the formation of another layered structure where the minority component layers are interrupted by channels through which the majority component layers are connected.[100] The structure is known as perforated layers ("pl") and despite an earlier assignment as an equilibrium phase it is now known to be in a long-lived metastable state.[101,102] In the vicinity of the "pl" phase another complex phase is formed. This phase possesses a bicontinuous structure ($Ia\bar{3}d$ symmetry) with the minority component forming two interpenetrating 3-fold coordinated networks, known as the gyroid phase ("gyr") (cf. Scheme 8A).[103] For more asymmetric compositions a hexagonal phase ("hex") is formed when the minority component forms hexagonally packed cylinders whereas the arrangement of the minority component in spheres packed in a body-centered cubic lattice is referred to as a spherical phase ("bcc").

Additional factors play an important role in determining the phase state: architecture,[104−108] fluctuation effects,[109,110] and conformational asymmetry.[111−114] The architecture, i.e., the way the unlike blocks are connected, was shown to have a strong effect on the phase behavior by changing the ODT temperatures and the boundaries between ordered phases.[104−108] Fluctuation effects raise the T_{ODT} and allow for direct transitions between the different ordered and disordered phases.[109] The main effect of conformational asymmetry is to shift the phase boundaries toward compositions richer in the segments with the higher asymmetry,[114] as shown by recent self-consistent field calculations.[111−114] The system poly(ethylene oxide-*b*-isoprene) (PI-*b*-PEO) is a unique system because of its high interaction parameter. Furthermore, the strong tendency of PEO to crystallize accounts for its unusual phase behavior. For example, a sample with $f_{\mathrm{PEO}} = 0.77$ and a molecular weight of about $M \approx 10^4$ shows five phases within about 200 K. Both PI and PEO have a similar glass transition temperature, $T_g \approx 200$ K, and therefore similar mobilities within the microphase. The extreme conformational asymmetry of PEO and PI is expected to affect the phase behavior.

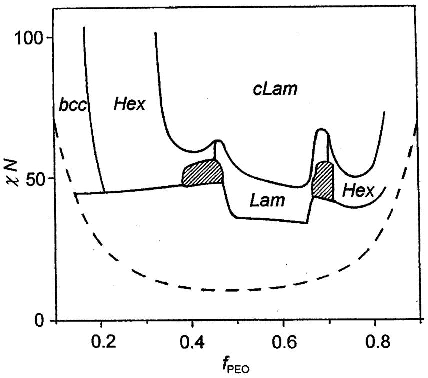

Figure 1. Phase diagram for the system poly(isoprene-*b*-ethylene oxide). The phase diagram is as follows: clam, crystalline lamellar; lam, amorphous lamellar; hex, hexagonal packed cylinders; shaded area, bicontinuous cubic structure (gyr). Only the equilibrium phases are shown which are obtained on cooling from high temperatures. The ODT and OOT temperatures were identified by SAXS and rheology. Values of χN were obtained by using $\chi N = 65/T + 0.125$. The dashed line gives the spinodal line in the mean-field prediction. Notice the pronounced asymmetry of the phase diagram with ordered phases shifted parallel to the composition axis. The asymmetric appearance can be accounted for by the conformational asymmetry of segments.

The phase behavior of PI-*b*-PEO has recently been extensively studied by Floudas et al.[115−117] A Flory interaction parameter (by fitting the disordered phase structure factor of the PI-*b*-PEO to the mean field theory predictions) of $\chi = 65/T + 0.125$ was found, and the corresponding transition temperatures were determined using small-angle X-ray scattering (SAXS) and rheological measurements. In conclusion, a phase diagram based on 25 samples spanning the range $0.05 < f_{\mathrm{PEO}} < 0.8$ depicted in Figure 1 was constructed.

The phase space of PI-*b*-PEO consists of five ordered phases: crystalline lamellar ("clam"), amorphous lamellar ("lam"), cylinders packed in a hexagonal lattice ("hex"), spheres in a body-centered cubic lattice ("bcc"), and the Gyroid ("gyr") phase with a $Ia\bar{3}d$ space group symmetry. The clam phase dominates the phase behavior at intermediate and strong segregations. The lam phase has a peculiar appearance owing to the clam formation at intermediate segregation. The gyr phase is found on both sides of the phase diagram, being the

Scheme 5. Schematic Drawing of Templin's Approach for Synthesizing Ordered Hybrid Materials: Left, Morphology of the Precursor Polymer; Right, Resulting Morphologies after Addition of Various Amounts of Metal Alkoxides

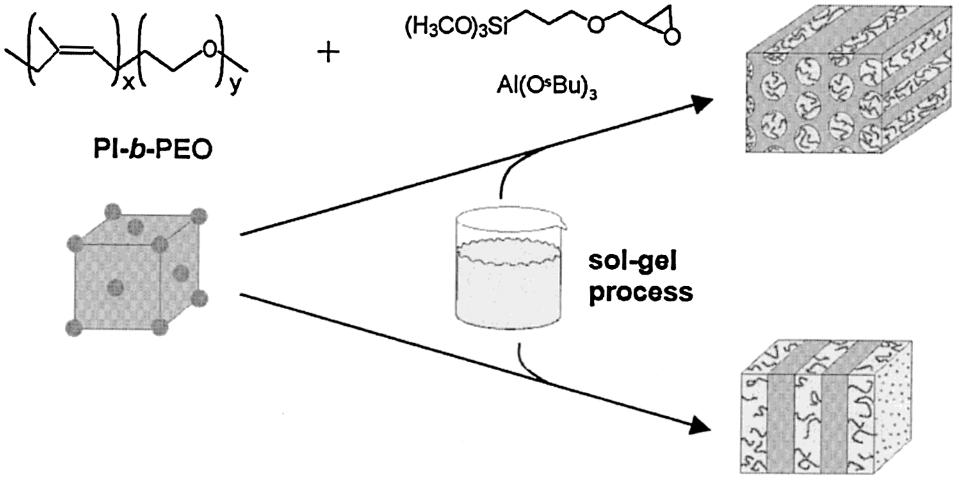

Table 1. Molecular Characteristics and Phase State of PI-*b*-PEO Block Copolymers and Structured Hybrid Materials Derived from Them

parent block copolymer name	M_n (PI)[a]	M_n (PEO)[b]	M_n (block)[c]	M_w/M_n[a]	f_{PEO}[b]	morpholgy[d]	hybrid material name	w_{INORG}	morphology[d]
PP3	8400	1500	9900	1.05	0.15	bcc			
							PP3/4	0.33	hex
							PP3/10	0.53	lam
PP5	12400	1800	14200	1.06	0.13	bcc			
							PP5/1	0.23	bcc
							PP5/2	0.32	hex
							PP5/3	0.45	lam
							PP5/4	0.65	inv. hex
							PP5/5	0.82	worm mic
							PP5/6	0.28	inv. bcc
PP7	28900	5200	34100	1.03	0.15	bcc			
							PP7/1	0.30	hex
PP9	10200	6200	16400	1.07	0.38	hex			
							PP9/1	0.53	lam
							PP9/2	0.56	PLN
							PP9/3	0.73	inv. hex
							PP9/4	0.79	inv. bcc
PP0	77400	6700	84100	1.05	0.080	bcc			
							PP0/3	0.28	hex

[a] From SEC. [b] From ^{1}H-NMR. [c] Calculated as M_n(block) = M_n(PI) + (M_n(PEO). [d] SAXS and TEM results.

last before disordering. For some volume fractions the hex phase has direct access to the disordered state. Due to the asymmetric compositions employed here, the bcc phase was only found on one side of the phase diagram. The phase diagram allows for direct transitions between the hex and gyr phases for $0.38 < f_{\mathrm{PEO}} < 0.46$ and between the lam and gyr phases on cooling diblocks with compositions in the range $0.66 < f_{\mathrm{PEO}} < 0.7$.[115,116] It is shifted along the composition axis toward the component possessing the more asymmetric segments. As a result, the gyr structure is observed for $0.4 < f_{\mathrm{PEO}} < 0.45$, with the upper bond being the highest composition ever reported.

3.2. Poly(Isoprene-*b*-Ethylene Oxide) Block Copolymers as Structure-Directing Agents in Sol–Gel Processes. When using block copolymers as structure-directing agents in sol–gel processes, one possible pathway toward structural control depends on the ability of the inorganic oxides to selectively swell only *one* block of the block copolymer. In the case of the GLYMO–Al(O^{s}Bu)$_3$ system, the aluminosilicate is expected to preferentially swell the hydrophilic PEO block. Consequently, Templin et al.[53] performed a sol–gel experiment by adding a mixture of prehydrolyzed GLYMO/Al(O^{s}Bu)$_3$ solution and KCl to a solution of PI-*b*-PEO in THF/CHCl$_3$. The entire process is sketched in Scheme 5, the characteristics of the block copolymers used are summarized in Table 1.

3.2.1. One-Dimensional Small-Angle X-ray Scattering. The structure-directing effect of the PI-*b*-PEO was highlighted in the following experiments: Three PI-*b*-PEO block copolymers with molecular weights of $M \approx 9.9 \times 10^3$ g/mol (PP3), 1.4×10^4 g/mol (PP5), and 3.4×10^4 g/mol (PP7) and a narrow molecular weight distribution ($M_w/M_n \leq 1.1$ leading to $M_w \approx M_n \approx M$) were employed in the sol–gel process (cf. Table 1 for characteristics of different block copolymers used). The microdomain structures of the resulting hybrid materials dependent on the weight fraction of the aluminosilicate, w_{INORG}, were investigated by small-angle X-ray scattering (SAXS). The resulting patterns at room temperature are depicted in Figure 2.

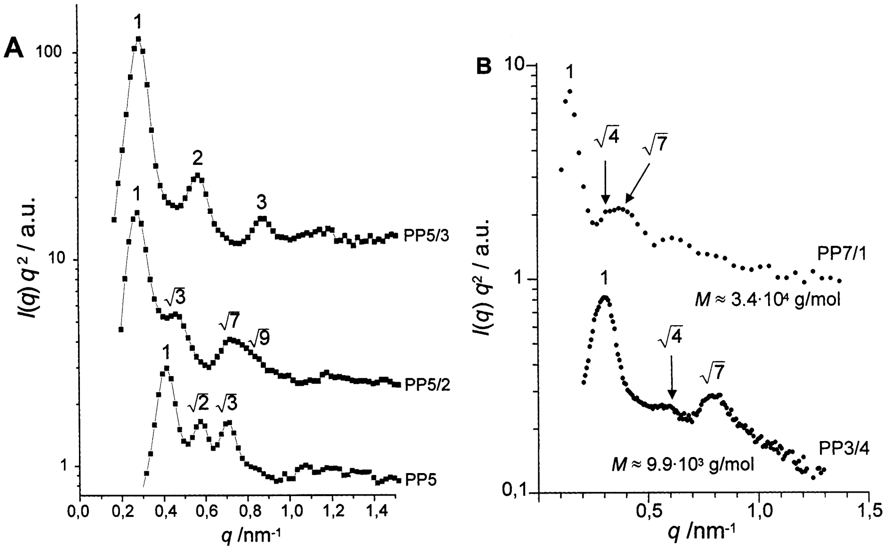

Figure 2. SAXS patterns of hybrid materials: (A) Block copolymer PP5 ($M = 1.4 \times 10^4$ g/mol, $f_{\mathrm{PEO}} \approx 0.13$; bcc) with different amounts of inorganic material, $w_{\mathrm{INORG}} = 0.32$ (PP5/2; hex), and $w_{\mathrm{INORG}} = 0.45$ (PP5/3; lam). (B) Effect of block copolymer molecular weight on hexagonal morphology at a given amount of inorganic material, $w_{\mathrm{INORG}} \approx 0.31$, $M = 9.9 \times 10^3$ g/mol (PP3/4), and $M = 3.4 \times 10^4$ g/mol (PP7/1) (hex). Angular positions of higher order peaks with respect to the first-order maximum are indicated for each curve.

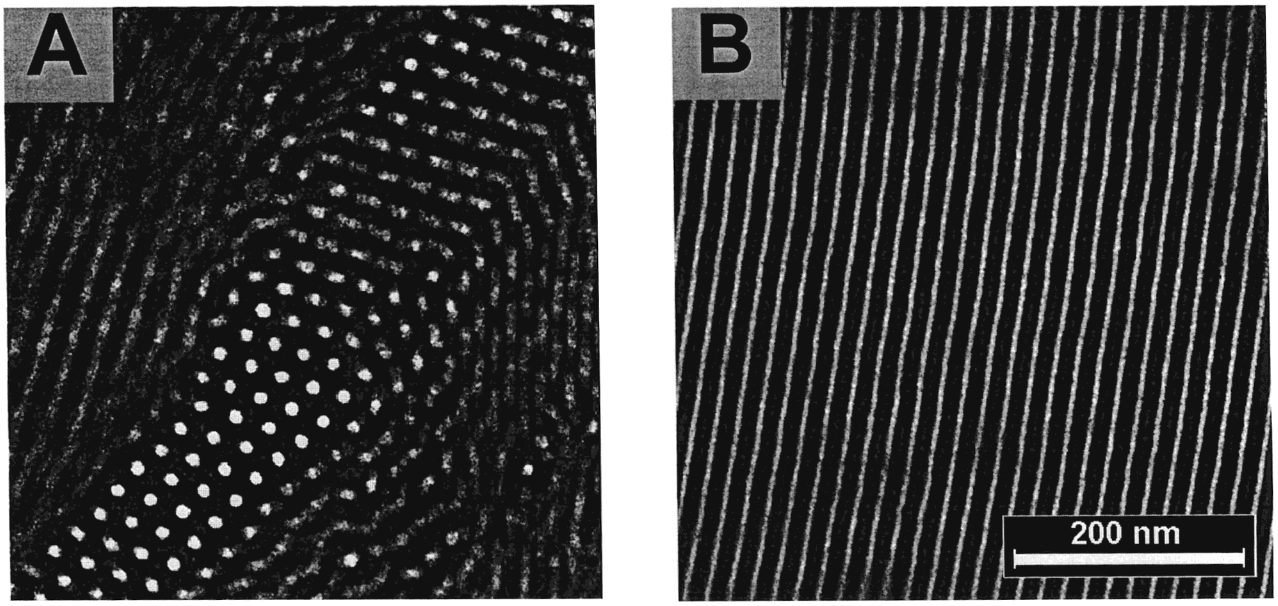

Figure 3. TEM micrographs of hybrid materials composed of PI-*b*-PEO PP5 ($M = 1.4 \times 10^4$ g/mol $f_{\mathrm{PEO}} \approx 0.13$) with (A) $w_{\mathrm{INORG}} = 0.32$ (PP5/2) and (B) $w_{\mathrm{INORG}} = 0.45$ (PP5/3), all at the magnification indicated by the bar in (B). Samples having a PI matrix were stained with OsO_4 before and after ultrathin sectioning. Images of stained specimens were taken under bright field conditions (energy loss $\Delta E = 0$, dark phase is stained PI).

For the pure PP5, the pattern with at least two higher order reflections at angular positions of $\sqrt{2}$ and $\sqrt{3}$ of the first-order maximum is characteristic for spheres packed in a simple or body-centered cubic lattice (bcc) (cf. Figure 2A). The composite material PP5/2, however, consisting of the same copolymer PP5 and metal oxides at a weight percentage of $w_{\mathrm{INORG}} = 0.32$, shows higher order reflections at angular positions of $\sqrt{3}$, $\sqrt{7}$, and $\sqrt{9}$. This spacing sequence is indicative of a hexagonal array of cylinders (hex). At an even higher amount of inorganic materials (PP5/3, $w_{\mathrm{INORG}} = 0.45$), two higher order reflections at integer multiples of the q value of the first-order peak are clearly visible. Such a sequence is characteristic of an arrangement of lamellae (lam) (cf. Figure 2A).

The effect of molecular weight of PI-*b*-PEO on the spacing of the resulting hybrid materials is outlined in Figure 2B. Both SAXS patterns are consistent with a hexagonal morphology at an aluminosilicate weight fraction of $w_{\mathrm{INORG}} \approx 0.31$. In the case of the PI-*b*-PEO of lower molecular weight (PP3 $M \approx 9.9 \times 10^3$ g/mol) the main peak is located at a q value corresponding to a spacing of ≈20.3 nm. In the composite prepared from the block copolymer with a higher molecular weight of $M = 3.4 \times 10^4$ g/mol, the spacing increases to ≈ 40 nm, indicating that not only the *morphologies* but also the *dimensions* of the structured hybrid materials can be fine-tuned on the nanometer scale.

3.2.2. Transmission Electron Microscopy. To corroborate the assignments of these SAXS patterns to the

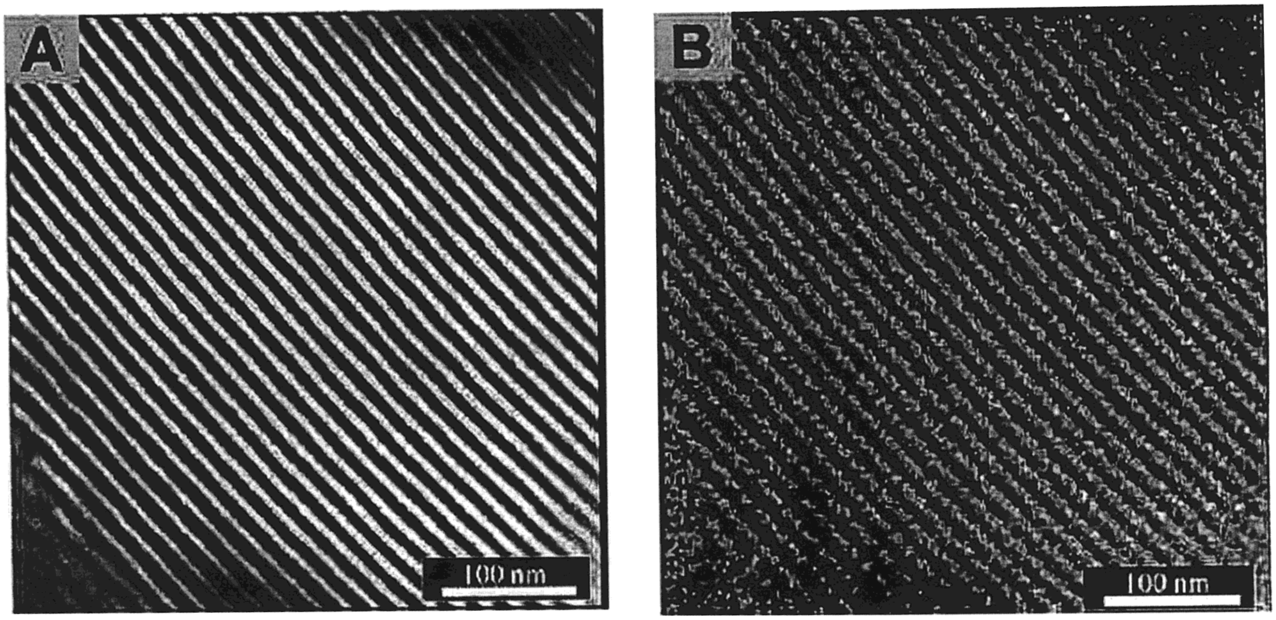

Figure 4. TEM micrographs of hybrid material PP3/10 (lam, $w_{\mathrm{INORG}} = 0.53$) reordered (A) in the energy-filtering imaging mode using electrons of zero energy loss and (B) using the method of elemental mapping as described in the text.

hex and lam morphology, samples were examined by transmission electron microscopy (TEM). The contrast in the micrographs arises from the PI phase, stained with OsO_4 and appearing black. The TEM image of the sample PP5/2 (cf. Figure 2A) clearly shows hexagonally packed cylinders (hex) in the two most typical projections (Figure 3A). The TEM of the sample PP5/3 with a higher amount of inorganic proves the lamellar structure (lam, Figure 3B).

Furthermore, the elemental mapping technique[118–120] was used to determine whether the silica-type material is confined to one phase of the block copolymer,[53] as expected. In this process two images are acquired at electron energy losses before the Si−$L_{2,3}$ edge and these are used to extrapolate an image expected at the energy loss of the Si−$L_{2,3}$ edge. Because the extrapolated image is not influenced by the absorption edge, it represents a silicon-nonspecific mass-thickness background. This background is then subtracted from a third image acquired at the Si−$L_{2,3}$ edge and the difference image represents the pure contribution of silicon to the contrast,[118] with areas containing silicon appearing bright. In Figure 4 two TEM micrographs of hybrid material PP3/10 ($w_{\mathrm{INORG}} = 0.53$) of an identical area are depicted. Figure 4A shows results obtained in the energy-filtering imaging mode using electrons of zero energy loss,[121] whereas in Figure 4B the same site was recordered using the elemental mapping technique. From these two micrographs (Figure 4) it is obvious that the inorganic silicon-rich phase has lamellar morphology and that the silicon is confined to the PEO phase.

3.2.3. Two-Dimensional Small-Angle X-ray Scattering. Due to the solvent cast technique,[122–124] which is part of the sample preparation, the hybrid material may exhibit a preferential orientation. Templin et al.[53] investigated this effect by using two-dimensional SAXS. The patterns of the lamellar sample PP3/10 ($w_{\mathrm{INORG}} = 0.53$) are depicted in Figure 5 for two different orientations with respect to the X-ray beam.

According to Figure 5, only a ring of small scattering intensity is observed in the q_x−q_y plane (film plane), whereas in the q_y−q_z plane two strong and narrow scattering peaks along q_z are detected. This result is expected for lamellae oriented parallel to the film surface. It demonstrates that the solvent cast technique is capable of producing macroscopically aligned samples in the case of lamellar silica type mesostructures.

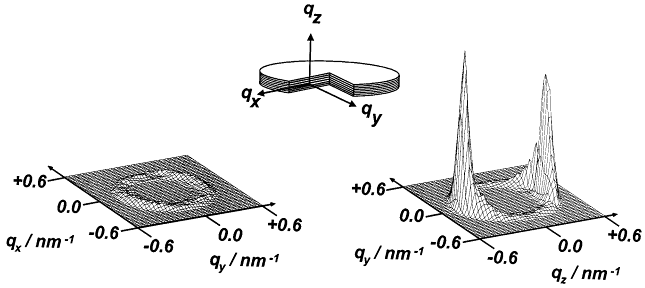

Figure 5. Two-dimensional SAXS patterns of hybrid material PP3/10 (lam, $w_{\mathrm{INORG}} = 0.53$), at 295 K for two different directions of the X-ray beam with respect to the sample coordinate frame, as schematically depicted in the inset.

3.3. Characterization of Structured Hybrid Materials by Solid-State NMR Techniques. While small-angle X-ray scattering (SAXS) and transmission electron microscopy (TEM) experiments explored the nanoscale morphologies, the molecular-level structure and dynamics as well as the nature of the hybrid material's aluminosilicate/PI-*b*-PEO interface remained an open question. In several other structured compounds, the inorganic phase was shown to be stabilized by Coulombic interactions with either the organic template[125] or with an intermediary counterion.[11] For the aluminosilicate/PI-*b*-PEO system, however, the situation is quite different since the separation of inorganic and organic regions is not as clearly defined. GLYMO itself contains both organic and inorganic moieties (cf. Scheme 3), and the intrinsic compatibility between GLYMO and PEO leads to a case where the organic polymer may significantly penetrate the aluminosilicate network as described for copolymer and epoxy resin mixtures.[126,127]

Scheme 6. Two Possible Models for the Distribution of the Aluminosilicate Network in the PEO Phase of PI-*b*-PEO; (A) Three-Phase Scenario: Interfacial Layer or *Interphase* of Pure PEO Is Present; (B) Two-Phase Scenario: Aluminosilicate Network Is *Distributed* throughout the PEO Phase

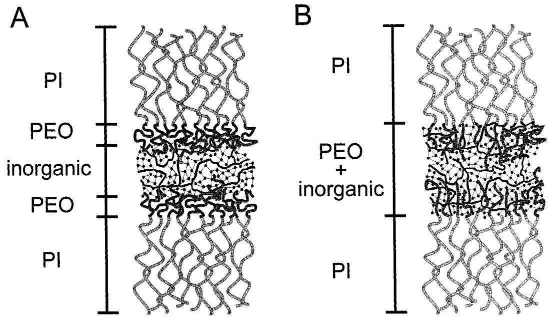

3.3.1. Possible Structural Models. Possible models for the distribution of the aluminosilicate component in the PEO phase of the lamellar composite (see Scheme 6) can be postulated analogously to previously studied block copolymer/homopolymer systems.[128−130] Theoretical studies of the addition of a homopolymer (A) to a block copolymer (AB) suggest that two competing effects control the location of the homopolymer within one of the phases of a lamellar block copolymer.[131] Covalent links between the blocks tend to pull the A-type monomer units of the block copolymer toward the B blocks (leaving the added homopolymer in the center of the A block), while entropic considerations favor a uniform distribution of the homopolymer throughout the A block. The size of the homopolymer tends to determine which scenario is most likely. For larger molecular weights of the homopolymer, covalent effects govern the system; for small molecular weights, the entropic effects dominate. Such effects have been observed experimentally.[128]

The aluminosilicate/PI-*b*-PEO hybrid system can be expected to behave similarly to such block copolymer/homopolymer systems since the aluminosilicate phase, which contains PEO-like organic segments, is selectively added to one block (cf. Figure 3). However, the effective "size" of this aluminosilicate layer is unknown. Two limiting scenarios are, therefore, possible. The first is an interfacial layer of pure PEO lying between the PI and the PEO/aluminosilicate mixture (Scheme 6A). In this case, PEO forms an interphase[132] and *three separate domains* can be distinguished ("three-phase scenario"). The second possibility is the aluminosilicate fully penetrating the PEO region of the block copolymer. Thus, there is no pure PEO layer, and the hybrid can adequately be described as a *two-phase system* ("two-phase scenario", Scheme 6B). Note that, in both cases, the separation of the PI from the PEO is expected to be sharp (less than 5 Å) because of the inherent incompatibility of these two polymers.[115]

3.3.2. Solid-State NMR Results. To verify these models and to obtain better insight into structure and dynamics of these novel structured hybrids in general, ^{1}H, ^{13}C, ^{27}Al, and ^{29}Si solid-state NMR measurements were performed by De Paul et al.[133]

Single-pulse ^{27}Al MAS NMR spectra in the presence and in the absence of the structure-directing PI-*b*-PEO are shown in Figure 6A. In both samples tetrahedrally (at $\delta = 55.2$ ppm incorporated into the aluminosilicate lattice[65]) and octahedrally (at $\delta = 5.4$ ppm, aluminumoxohydroxo domains,[64,75] $AlO_x(OH)_y(H_2O)_z$) coordinated aluminum species were found, cf. Scheme 4. Significantly, in contrast to the unstructured hybrids, no peak was present in the 30−40 ppm region, where highly distorted tetrahedral sites are expected to resonate. This indicates that for the structured hybrids no significant numbers of severely distorted aluminum sites in the aluminosilicate network are present. The relative intensities of the sites varied when comparing the unstructured with the structured hybrid materials of different polymer/inorganic compositions but no systematic relation to composite morphology was observed.[133]

Further information about the inorganic part was obtained from ^{29}Si NMR (Figure 6B). Again, the two spectra of the structured and unstructured material are qualitatively similar to each other, as peaks due to T^1, T^2, and T^3 sites can be clearly distinguished in both spectra. The downfield peak at −46.5 ppm (clearly visible in the upper spectrum, but also present in the lower one) can be attributed to a specific T^3 environment $RSi(OAl)_3$ in which the silicon is coordinated via bridging oxygens to three aluminums. When ^{29}Si NMR spectra of structured hybrids with different amounts of inorganic material are compared, the populations of the

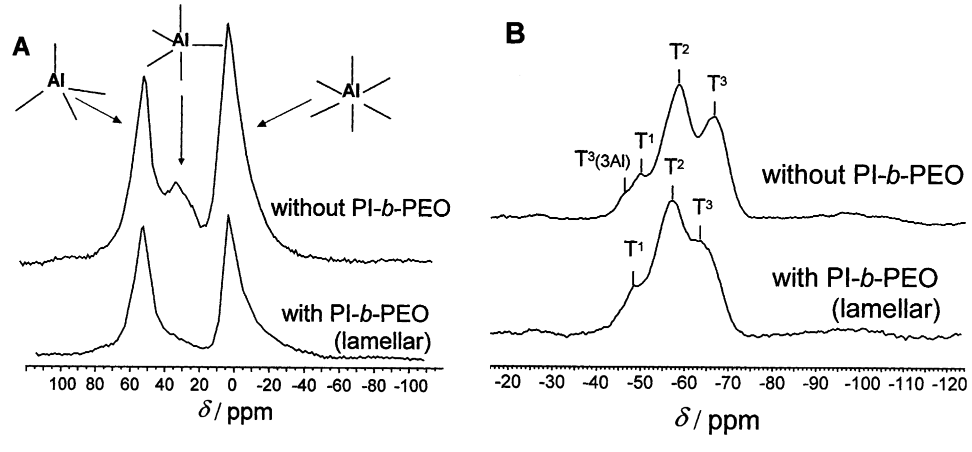

Figure 6. Comparison of the MAS NMR spectra of the structured (sample PP5/3, lam) and the unstructured hybrid material: (A) ^{27}Al MAS NMR spectra and (B) the ^{29}Si MAS NMR spectra. Chemical shifts in ppm from $AlCl_3$ and TMS, respectively.

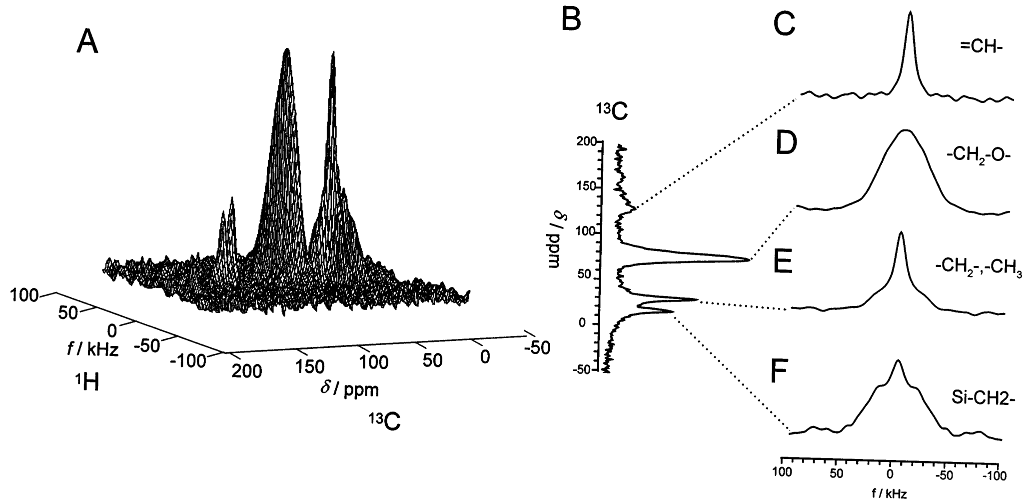

Figure 7. Results of a two-dimensional WISE experiment performed on the lamellar composite PP5/3. Chemical shifts in ppm from TMS. (A) A stacked plot of the full spectrum. (B) The projection along the ^{13}C dimension. Proton slices corresponding to (C) the vinyl protons in PI, (D) the $-CH_2O-$ protons in PEO and GLYMO, (E) the aliphatic protons, found throughout the composite, which are not near oxygen or silicon, and (F) the $-CH_2-Si-$ protons in GLYMO. Larger proton line widths correspond to more rigid regions of the sample.

various silicon environments do not significantly change as a function of composite morphology.[133] In fact, the observed differences likely reflect normal fluctuations in the hydrolysis step.

These results indicate that the polymer is not likely to play a significant role in the inorganic network formation since the NMR spectra of the structured and unstructured hybrid materials are very similar.

3.3.3. Local Dynamics as Revealed by Two-Dimensional Wide-Line Separation Spectroscopy (WISE) and Differential Scanning Calometry (DSC). On the other hand, the inorganic components are expected to influence the dynamics of the block copolymer, respectively the PEO block. In fact, one common reason for forming organic–inorganic composites is to improve the hardness of the polymeric materials.[51] To find out whether the PEO/aluminosilicate phase is uniformly rigidified or a distribution of mobilities exists, two-dimensional wide-line separation spectroscopy[134,135] (WISE) experiments were performed.[133] This technique gives insights into the relative mobilities as large proton width corresponds to more rigid regions of the sample. Figure 7 shows the results of a WISE experiment performed on the lamellar composite PP5/3 (lam) at 268 K. (The sample was cooled to reduce the mobility of the polyisoprene so that cross polarization was possible.)

Dynamic differences in mobility for the different regions of the sample were observed. The vinyl protons (Figure 7C, occurring exclusively in polyisoprene) were quite mobile. The least mobile protons were associated with the carbons adjacent to oxygen (Figure 7D, found in poly(ethylene oxide) and GLYMO) and with the carbons adjacent to silicon (Figure 7F, found exclusively in GLYMO), respectively. The aliphatic proton line (Figure 7E), made up of contributions from the methylene groups in polyisoprene and in GLYMO as well as the methyl groups in polyisoprene and in one of the minor hydrolysis products of GLYMO (cf. Scheme 3) had two clear components: a broad component and a narrower component. The mobile component is naturally assigned to polyisoprene. These results indicate the presence of significant dynamical heterogeneity in the composite materials. In particular, the polyisoprene is quite mobile, while both the PEO and GLYMO phases are significantly more rigid. The glass transition of PI as measured by DSC is, in fact, the same in the composites as in the pure block copolymer ($T_g \approx 214-215$ K, compare Figure 8). The behavior of the PEO

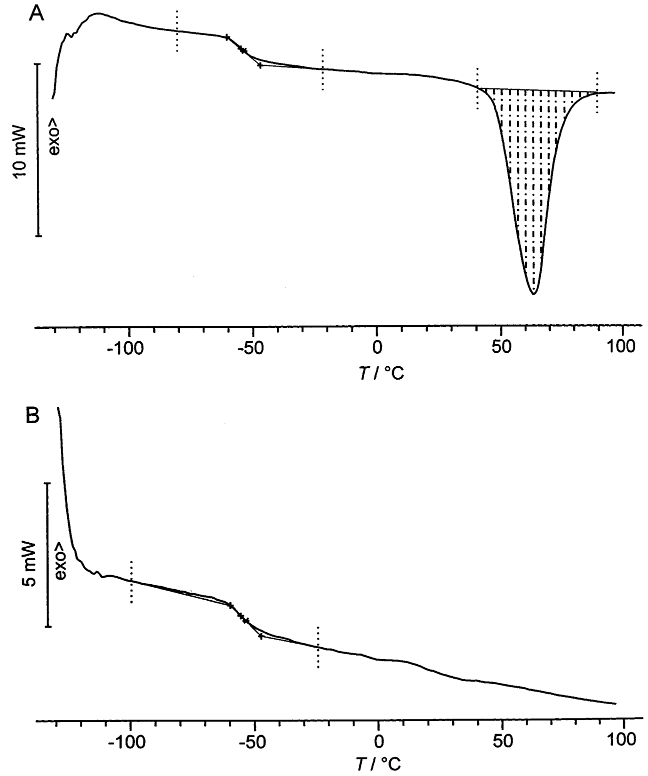

Figure 8. DSC traces of (A) the pure PI-*b*-PEO copolymer and (B) the lamellar composite PP5/3 ($w_{INORG} = 0.53$). The glass transition temperature of the PI in the composite ($T_g \approx 215$ K) is approximately unchanged from that of the bulk ($T_g \approx 214$ K). The concentration of PEO is too low ($f_{PEO} = 0.13$) to permit observation of its glass transition in any of the materials. Note that a melting peak at 315 K is clearly evident in the DSC of the pure block copolymer and indicates the presence of crystalline PEO; such a peak is absent from all the composite materials.

phase, however, is dramatically different in the composites as compared to that in the bulk block copolymer. Unfortunately, the glass transition of PEO in these systems (expected to occur somewhere in the range 158−233 K[136]) is too weak to be detected. However, while the pure block copolymer shows a strong melting peak (see Figure 8A), crystallization of PEO is entirely suppressed in the composites (see Figure 8B). This provides evidence for significant mixing of the inorganic and PEO phases. It is interesting to note that composites with higher PEO volume fractions (up to 35%) also fail to show a melting peak.

3.3.4. Interface between the Organic/Inorganic Hybrid and Organic Regions. The presence of dynamic heterogeneity in the lamellar composite suggests the possibility of using differences in mobility as a way to selectively excite magnetization in certain regions of the composite. More specifically, one could apply a "mobility filter" to suppress the signal from the less mobile spins and then monitor the diffusion of magnetization from the mobile to the immobile regions of the sample. Since the rate of spin diffusion is related to internuclear distances, such experiments allow the length scales in the sample to be determined.[67,132,137,138] The ^{13}C detected spin-diffusion NMR experiment consists of four basic steps:[139,140] (i) a dipolar filter step which suppresses the ^{1}H magnetization of rigid parts of the sample, (ii) a "mixing" step (characterized by a mixing time, t_m) in which the remaining magnetization spreads to neighboring spins, (iii) a transfer step in which ^{1}H magnetization is transferred to the nearest ^{13}C spins, and (iv) a detection period in which resolved ^{13}C signals are recorded.

As discussed above, the PEO/aluminosilicate phase is more rigid than the PI part. Thus, at the beginning of the "mixing step", only polyisoprene protons have a net magnetization. During the mixing time, this magnetization is transferred at a rate proportional to $1/r_{ij}^3$ (in abundant proton spin systems) by a process known as "spin diffusion". At short mixing times, polarization is only transferred to spins near the magnetization source; at longer times, relayed transfer can occur. After the mixing period, a short cross-polarization step is used to monitor the location of the magnetization that has "diffused" throughout the sample.

Figure 9 shows the intensity of the $-Si-CH_2-$ carbon peak (i.e., the GLYMO containing regions of the sample) in the lamellar sample PP5/3 as a function of mixing time.[67,133,137] Intensities were corrected for the proton spin−lattice relaxation time T_1 and normalized to the plateau value (the average of the last 6 data points). A linear fit to the first 11 data points gave a slope of $0.12 \pm 0.01 \times 10^{-3}$ s$^{-1/2}$ and a *y*-intercept of 0.0 ± 0.04. From these values, the *x*-intercept was found to be $0.0 \pm 0.5 \times 10^{-3}s^{1/2}$. If there were a PEO interphase (cf. Scheme 6A), magnetization would initially diffuse from the isoprene to this PEO phase. Only at later times would it reach the GLYMO protons. Such a situation would correspond to a spin-diffusion buildup plot for the GLYMO carbon, which has an *x*-intercept that is greater than zero.

The absence of such a "lag time" like in Figure 9 indicates that the model of Scheme 6B, where PEO and GLYMO are intimately mixed, is representative of the system. Nevertheless, the presence of a small interfacial layer due to experimental error of the NMR experiments cannot be completely ruled out. The upper bound of this layer can be estimated from an error analysis to be 10 Å, i.e., 1 nm. This is small compared to the 9-nm thickness of the PEO/aluminosilicate layer as obtained from SAXS and TEM measurements on the sample PP5/3. Consequently, the model depicted in Scheme 6B is a superior description of the reality. Note that 1 nm is also significantly smaller than the mean-squared end-to-end distance of a freely rotating chain of PEO with M_n(PEO) = 1800 g/mol (see Table 1), $\langle r^2\rangle^{1/2} = 2.3$ nm, which can be taken to represent a lower bound for the size of a PEO-rich interphase if the model of Scheme 6A were correct.

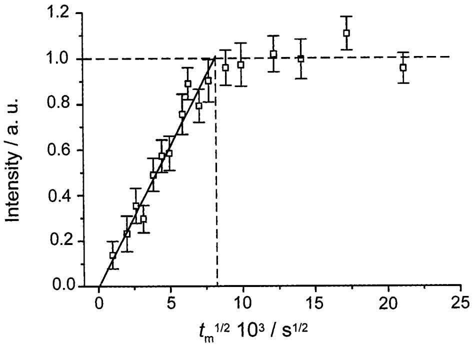

Figure 9. Intensity of the signal from the carbon adjacent to silicon as a function of the square root of the mixing time of the lamellar sample PP5/3 at 268 K. The solid line drawn through the data represents the best fit to the initial 11 points. The slope of this line is $0.12 \pm 0.01 \times 10^{-3}$ s$^{-1/2}$ and the *x*-intercept is $0.0 \pm 0.5 \times 10^{-3}$ s$^{-1/2}$, indicating that there is no significant interphase present between the polyisoprene and the inorganic part of the composite. The error bar represents the root-mean-square of the noise for each spectrum.

In summary, the behavior of the aluminosilicate network is in qualitative agreement with that of a low molecular weight homopolymer mixed with a block copolymer and the two-phase scenario depicted in Scheme 6b describes the situation quite well. It is interesting to note that this mesoscopic structure is in striking contrast to what is observed in other approaches toward block copolymer derived silica-type materials.[141] While these methods are limited, in the following it will be shown that the present strategy allows access to the entire phase space of block copolymers for the design of hybrid morphologies.

4. Exploring the Phase Space of Ormocer-Derived Organic−Inorganic Hybrid Materials

4.1. Morphologies Known from Organic Block Copolymers. In the last paragraph we showed that changing from conventional silicon precursors to *or*ganically *mo*dified *cer*amic (ormocer) precursors in the block copolymer directed synthesis leads to a unique polymer−ceramic interface in which the hydrophilic blocks of the amphiphilic copolymers are completely integrated into the ceramic phase. This "quasi-two-phase system" should allow for a more rational hybrid morphology design based on the current understanding of the phase behavior of block copolymers and copolymer−homopolymer mixtures.[50]

Scheme 7. Schematic Drawing of Ulrich's Approach to the Synthesis of Hybrid Materials Exhibiting Different Morphologies[a]

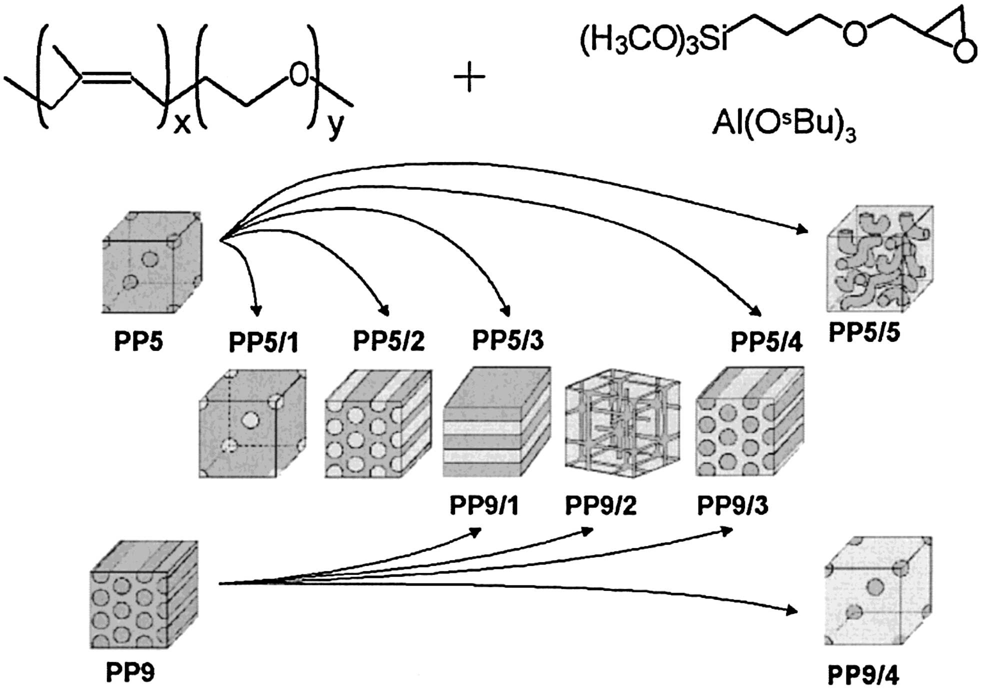

[a] See text and Table 1 for explanation of sample names.

Moreover, the morphology of the final hybrid material should mainly be a function of the weight fraction of the inorganic components and essentially be independent of the microstructure of the PI-*b*-PEO block copolymer. As will be shown below, this allows access to a wide variety of morphologies starting from a single-block copolymer by simply mixing in the inorganic components. The effect of increasing ormocer content on the mesostructures was explored by Ulrich et al.[54,142] All results obtained so far are summarized in Scheme 7. Representative TEM micrographs of these hybrid morphologies are depicted in Figures 10 and 11, respectively.

Increasing the content of GLYMO and $Al(O^sBu)_3$ leads to spheres (PP5/1, $w_{INORG} = 0.23$, Figure 10A), hexagonally packed cylinders (PP5/2, $w_{INORG} = 0.32$, Figure 10B), lamellae (PP5/3, $w_{INORG} = 0.45$, Figure 10C), the inverse cylinder morphology (PP5/4, $w_{INORG} = 0.65$, Figure 10D), and randomly packed wormlike micelles of PI in an inorganic-rich matrix (PP5/5, $w_{INORG} = 0.82$, Figure 10E) when starting from the PI-*b*-PEO block copolymer PP5 with a bcc structure (1.4×10^4 g/mol, $f_{PEO} \approx 0.13$). Lamellae (PP9/1, $w_{INORG} = 0.53$), a bicontinuous cubic structure (PP9/2 $w_{INORG} = 0.56$, Figure 11 vide infra), an inverse cylinder morphology (PP9/3, $w_{INORG} = 0.73$), and inverse spheres (PP9/4, $w_{INORG} = 0.79$, Figure 10F) were found when employing the block copolymer PP9 exhibiting a hexagonal array of cylinders ($M = 16400$, $f_{PEO} = 0.38$) as the structure-directing agent.

When the sequence of hybrid morphologies in Scheme 7 are compared with that observed for the pure PI-*b*-PEO block copolymer in Figure 1 (or sequences found for other diblock copolymers[50]), the following issues arise. First, only with block copolymer PP9 could a bicontinuous cubic structure be obtained. As described below, SAXS and TEM data on this bicontinuous structure is not consistent with a double-gyroid morphology but rather suggests a so-called "Plumber's nightmare" morphology,[143,144] a phase first described within the organelles of certain plant cells.[19] Second, only with polymer PP9 could the inverse spherical morphology be reached through the addition of inorganic material. With block copolymer PP5 the addition of large amounts of inorganic material ($w_{INORG} > 0.8$) leads to wormlike rather than spherical micelles. This morphology has been reported for A_2B-mictoarm star polymers[145] and diblock copolymer/homopolymer (AB/A) mixtures.[128,146] The occurrence of wormlike micelles instead of spheres arranged on a cubic lattice has been ascribed to interphase-curvature constraints.[145] In summary, the fact that the use of block copolymers with different morphologies leads to slightly altered sequences of microstructures indicates subtle, yet poorly understood, differences in the phase behavior between the present hybrid materials and block copolymers. Despite these small differences, the overall structural control is tremendous, as also underlined by the quality of the data.

4.2. The Plumber's Nightmare Morphology. Complex bicontinuous cubic structures have always attracted particular attention of researchers in the past.[19] Besides their esthetic character, the right assignment of structures is a challenge. In Scheme 8A the real space image of a double-gyroid phase (of $Ia\bar{3}d$ symmetry) is shown, a structure now well established to exist in block copolymer materials.[50]

Finnefrock et al.[144] investigated the PI-*b*-PEO/aluminosilicate hybrid material morphology in an area of block copolymer phase space where such a gyroid phase was expected. To their surprise, their data were not consistent with those of a gyroid but rather suggested a "Plumber's Nightmare"[143] morphology (see Scheme 8B for the real space image). Their bright field TEM data

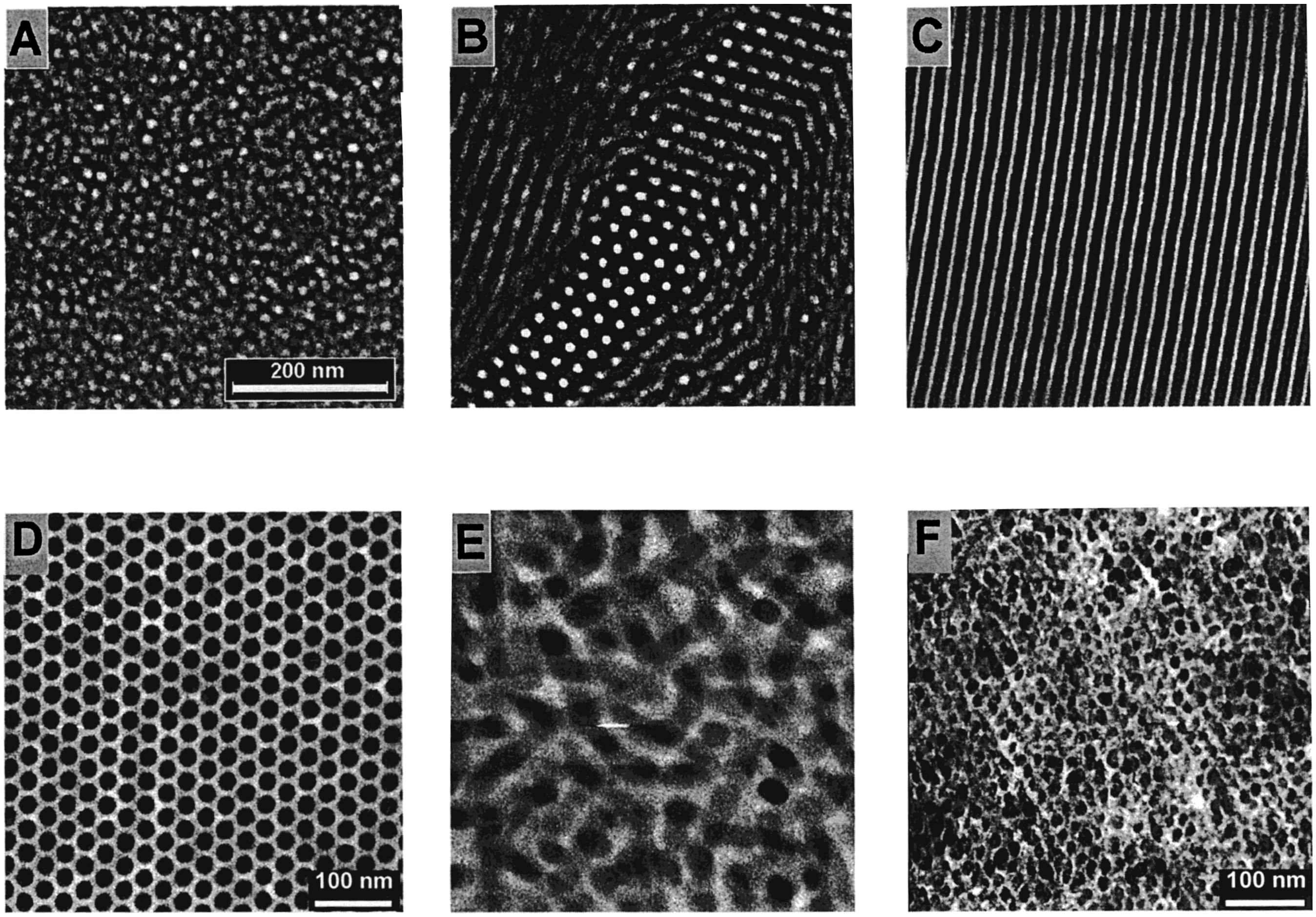

Figure 10. TEM micrographs of the hybrid materials (A) PP5/1 (bcc), (B) PP5/2 (hex), (C) PP5/3 (lam), (D) PP5/4 (inv. hex), (E) PP5/5 (wormlike micelles), and (F) PP9/4 (inv. bcc) shown all in the magnification indicated by the bar in (A), if not otherwise indicated. Bulk samples having a PI matrix were stained with OsO_4 before and after ultrathin sectioning. Images of stained specimens were taken under bright field conditions (energy loss $\Delta E = 0$ eV, dark phase is stained PI) while unstained ones (inorganic-rich matrix) were imaged utilizing structure-sensitive contrast ($\Delta E = 250$ eV, the silicon- and aluminum-containing phase appears bright). Hence, the PI and the aluminosilicate are generally shown as the dark and the bright phase, respectively.

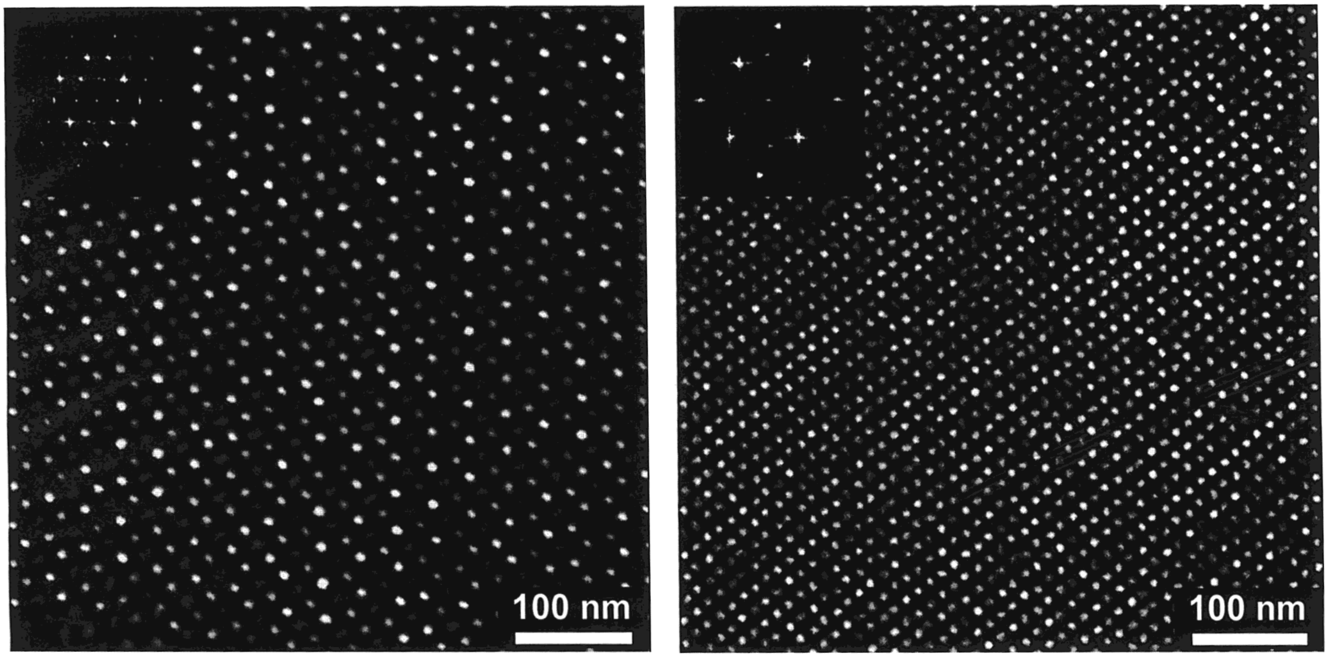

Figure 11. Bright field transmission electron microscopy (TEM) of the hybrid material PP9/2 exhibiting the plumber's nightmare phase, highlighting the 3-fold (left) and 4-fold (right) projections of the cubic phase. Insets to each panel show the computed Fourier diffraction patterns.

Scheme 8. Real Space Image of a Stick Structure Derived from a Plumber's Nightmare (B); for Comparison, the Real Space Image of a Gyroid (A) and That of a Double Diamond Derived Structure Are Shown in (C)[a]

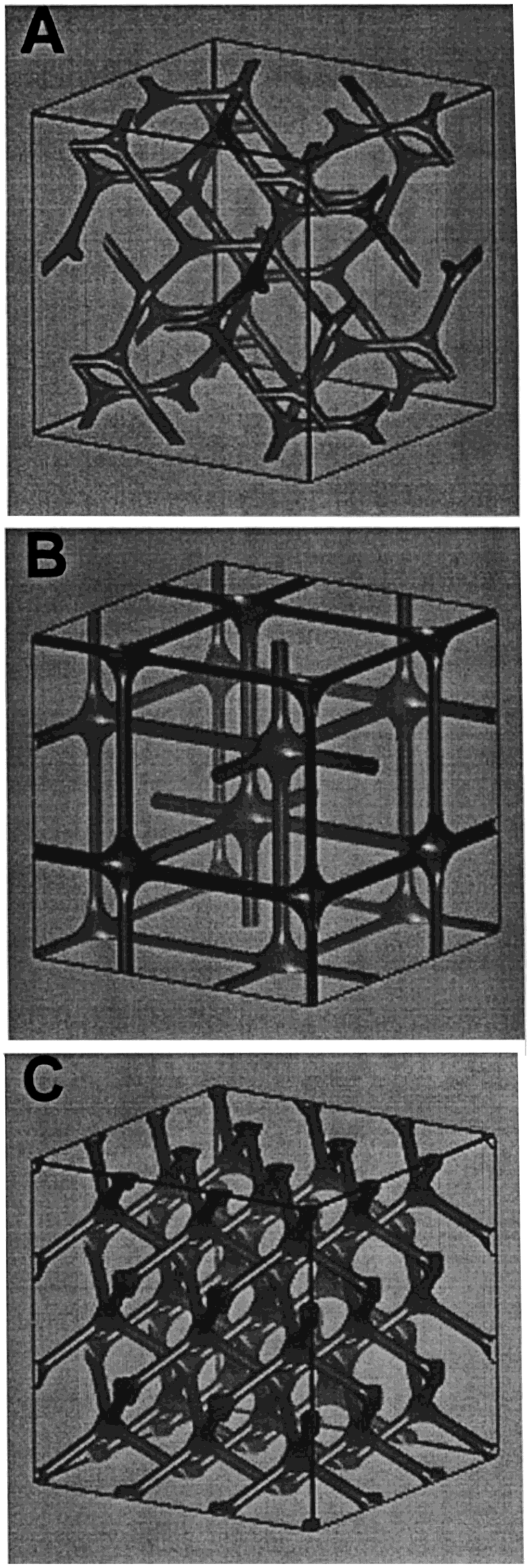

of sample PP9/2 ($w_{\mathrm{INORG}} = 0.56$) are depicted in Figure 11. Both micrographs show cubic 4-fold and 3-fold orientations as expected for cubic morphology. The connected volumes (channels) with 4-fold and 3-fold ("wagon-wheel") orientations, typical of a bicontinuous cubic structure, can be more easily identified in TEM data of calcined samples (see Figure 22). Furthermore, as demonstrated by scanning electron microscopy (SEM), the materials show a remarkably large average grain size (data not shown). It was not uncommon to find grains spanning the entire area of a grid mesh (approximately 100 μm in diameter).

The underlying symmetry and the long-range structure was further elucidated by SAXS experiments (Figure 12). The X-ray pattern indicates a remarkable degree of ordering, out to $q^2 = h^2 + k^2 + l^2 = 50$ reciprocal lattice units despite the structure being highly disordered on length scales of a few angstroms. Consistent with the large grain sizes observed by electron microscopy,[144] the distinct peaks in the images imply that the X-ray beam (<0.1 mm^2) averages only over a limited number of crystallites with different orientations. Using systematic algorithms, a structure was solved from each set of peaks that could originate from a single microdomain within the scattering volume. (see Figure 12b for peak positions)

The inclusion of azimuthal information on the SAXS pattern, such as that presented in Figure 12, places strong constraints on the possible symmetry groups and unit cell lengths of the sample. The reciprocal-space SAXS data are consistent with $Im\bar{3}m$ symmetry, and the lattice basis length can be determined to be 630 Å, consistent with the analysis of the TEM data. The TEM data, together with the X-ray $Im\bar{3}m$ symmetry, suggest a Plumber's Nightmare-like phase[143] and excludes the gyroid and double diamond (see Scheme 8c for a real space image of the latter).

5. Nanoengineering

In the previous paragraphs it was demonstrated that, despite subtle differences in the phase behavior of the present hybrid materials from that of conventional block copolymers, the ormocer approach allows access to a sequence of morphologies (by simply adding different amounts of inorganic material to the same block copolymer) that is very similar to that found in all-organic block copolymer systems. Indeed, a more rational hybrid morphology design than in the past is thus achieved. In the following section based on the bulk hybrid materials, pathways toward different potential applications will be highlighted, focusing on the preparation of isolated nano-objects of predetermined shape, size, and composition as well as on mesoporous materials. These approaches are schematically depicted in Scheme 9. While those bulk phases rich in PI can be utilized to obtain single, well-defined nano-objects, calcinations at elevated temperatures of those phases rich in inorganic material lead to mesoporous materials. The nano-objects have potential applications, e.g., as fluorescent markers in the area of biotechnology and nanobiotechnology while the mesoporous materials could find way into separation technology and catalysis.

5.1. Preparation of Isolated Nano-objects. In the hybrid materials with tailored morphologies (cf. previ-

[a] Graphics were generated using the following web site: http://msri.org/publications/sgp/SGP/. Gray scales serve to distinguish the two distinct three-dimensional channel systems in each case.

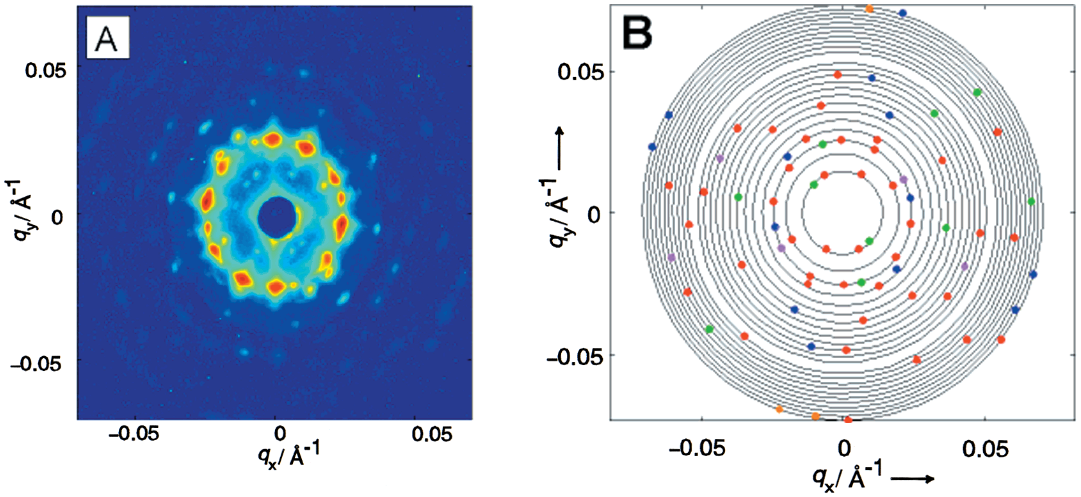

Figure 12. (A) SAXS image of the hybrid material PP9/2 exhibiting the plumber's nightmare phase. The false color scale (ascending from blue to red) corresponds to logarithmic X-ray intensity. (B) Indexed peak positions are shown on the right. Peaks from the same crystallite are colored identically. All these peaks can be assigned to five microdomains within the scattering volume. The circle radii are given by $q = (h^2 + k^2 + l^2)^{1/2}$, where h, k, l are integers allowed by the $Im\bar{3}m$ symmetry group. The apparent gap results because $q^2 = 28$ units is not the sum of any three squares of integers.

Scheme 9. Schematic Drawing for the Preparation of Nano-objects as Well as Mesoporous Materials[a]

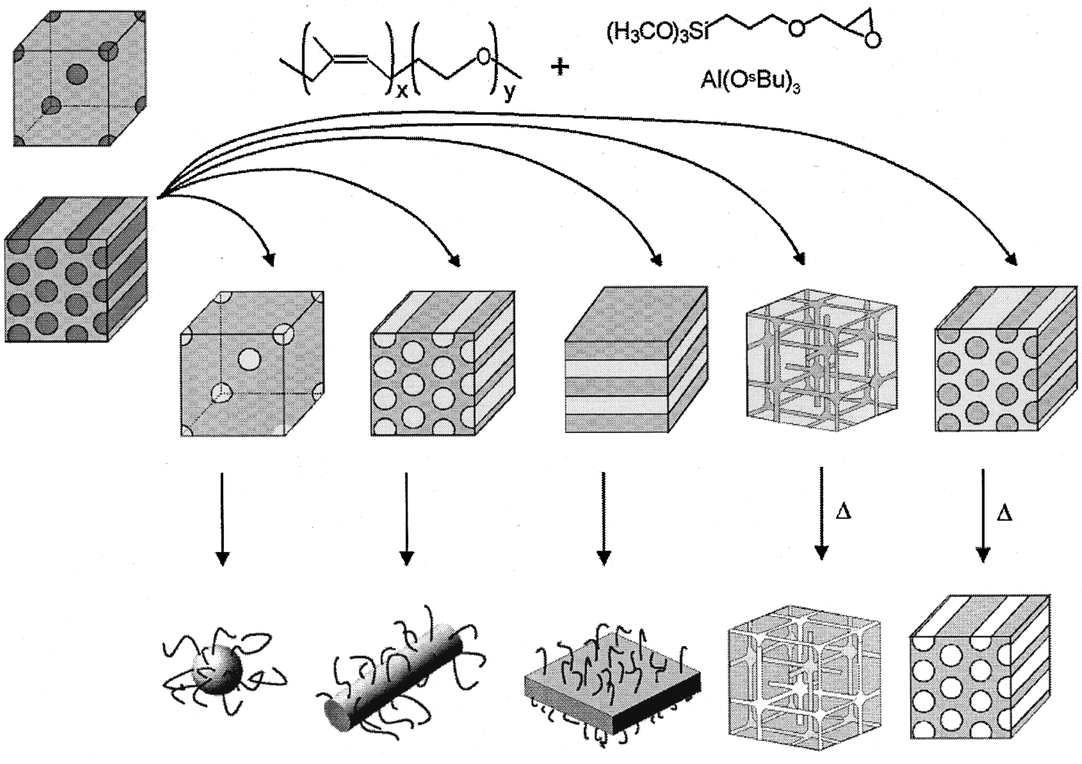

[a] Single "hairy" nano-objects of different shapes are isolated by dissolution. Calcinations at about 600 °C lead to mesoporous materials with preserved morphologies..

ous discussion) the condensation of the alkoxides leads to a covalent three-dimensional network incorporating the PEO block of the PI-*b*-PEO block copolymer. Thus, selective swelling of the purely organic PI ultimately leads to single, isolated hybrid objects of controlled shape and size (Scheme 9).

Ulrich et al.[54] used this approach to prepare hybrid spheres, cylinders, and plates from the respective bulk phases as evidenced by TEM (Figure 13).

As the hydrophilic PEO block of the copolymer acts as an anchor for the metal alkoxide condensation products, the copolymers remain partly embedded in the hybrid phase after dissolution. The nano-objects are therefore covered by a thin PI layer as evidenced in Figure 14 by using structure-sensitive contrast TEM measurements.[118,119,121]

Whereas the upper part of Figure 14 exclusively reveals the silicon- and aluminum-containing cylinder core (structure-sensitive contrast[118,119,121]), the lower part depicts the carbon distribution, clearly showing the organic polymer layer. Hence, the block copolymer is an integral part of the nano-objects. They can be described

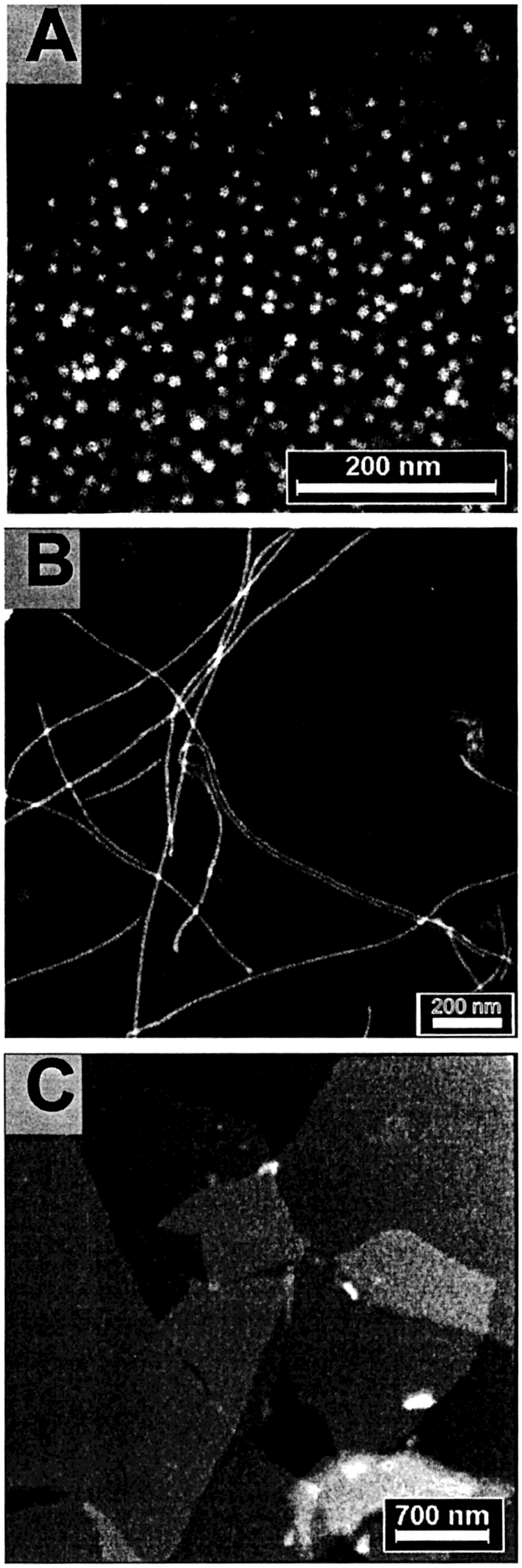

Figure 13. TEM micrographs of isolated nano-objects of different shapes. Samples were obtained by dissolution of the hybrid material in tetrahydrofuran, forming colloidal solutions that were stirred for about 1 week. They were then cast onto thin carbon films: (A) spheres prepared from PP5/1 (w_{INORG} = 0.23); (B) cylinders prepared from PP5/6 (w_{INORG} = 0.28); and (C) lamellae prepared from PP5/3 (w_{INORG} = 0.45). Micrographs were recorded using structure-sensitive contrast. Image (C) exhibits single plates that partially overlap. In the lower right corner at least four plates are stacked on top of each other.

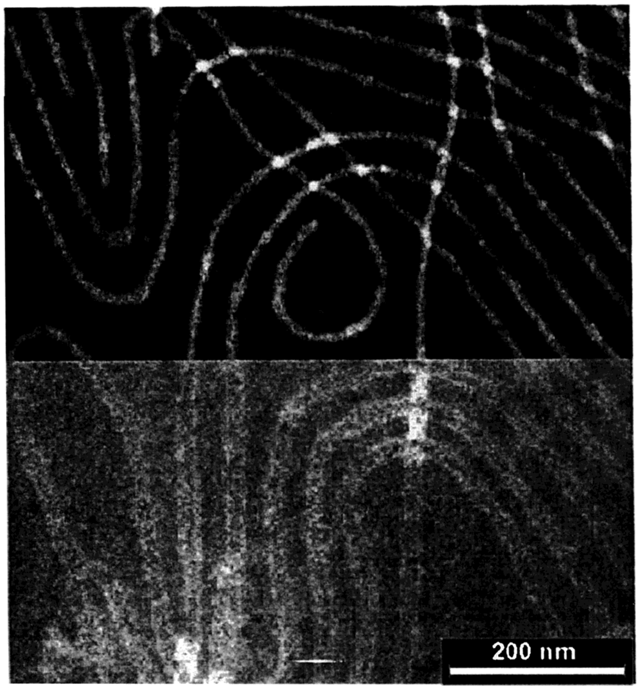

Figure 14. TEM picture of cylindrical nano-objects prepared by swelling the hybrid material PP5/3 (cf. Figure 13B) using structure-sensitive contrast in the upper part (Al−Si contrast) and the carbon map (carbon distribution image reordered using the C−K absorption edge, three window potential extrapolation[118,119,121]), clearly showing that the aluminosilicate cylinders are coated with a thin layer of block copolymer (the background intensity is due to the carbon film).

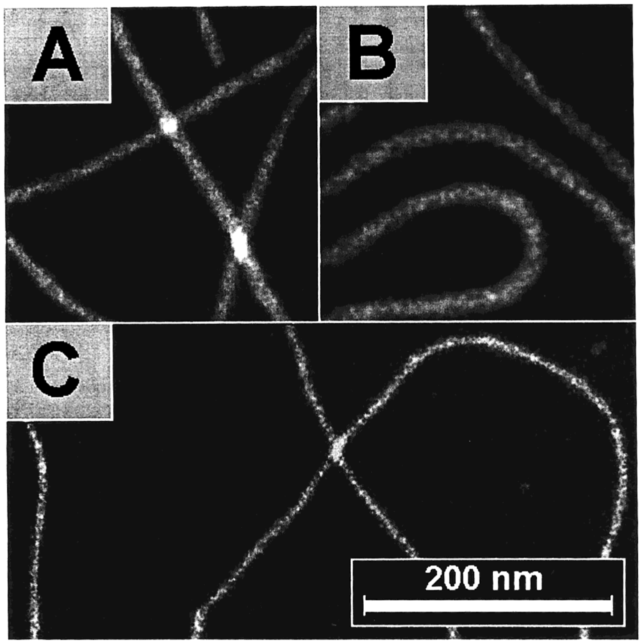

Figure 15. TEM micrographs of isolated cylinders with tailored properties. Effect of the amount of metal oxide and calicination: (A) isolated cylinders obtained by dissolution of PP5/2 (w_{INORG} = 0.32) with a diameter of 12.5 nm. (B) Isolated cylinders obtained by dissolution of PP5/6 (w_{INORG} = 0.28) with a diameter of 10.0 nm. This demonstrates the effect that an increasing amount of metal oxides, w_{INORG}, has on the diameter of the cylinders. (C) Ceramic objects obtained from the cylinders shown in (A) by the following procedure. First, the "hairy" cylinders were transferred to KCl plates. In a second step combustion of the organic parts under an oxygen atmosphere at 873 K was performed. Afterward, a detachment replica was prepared by evaporation of a thin carbon film that was floated off the KCl onto water.

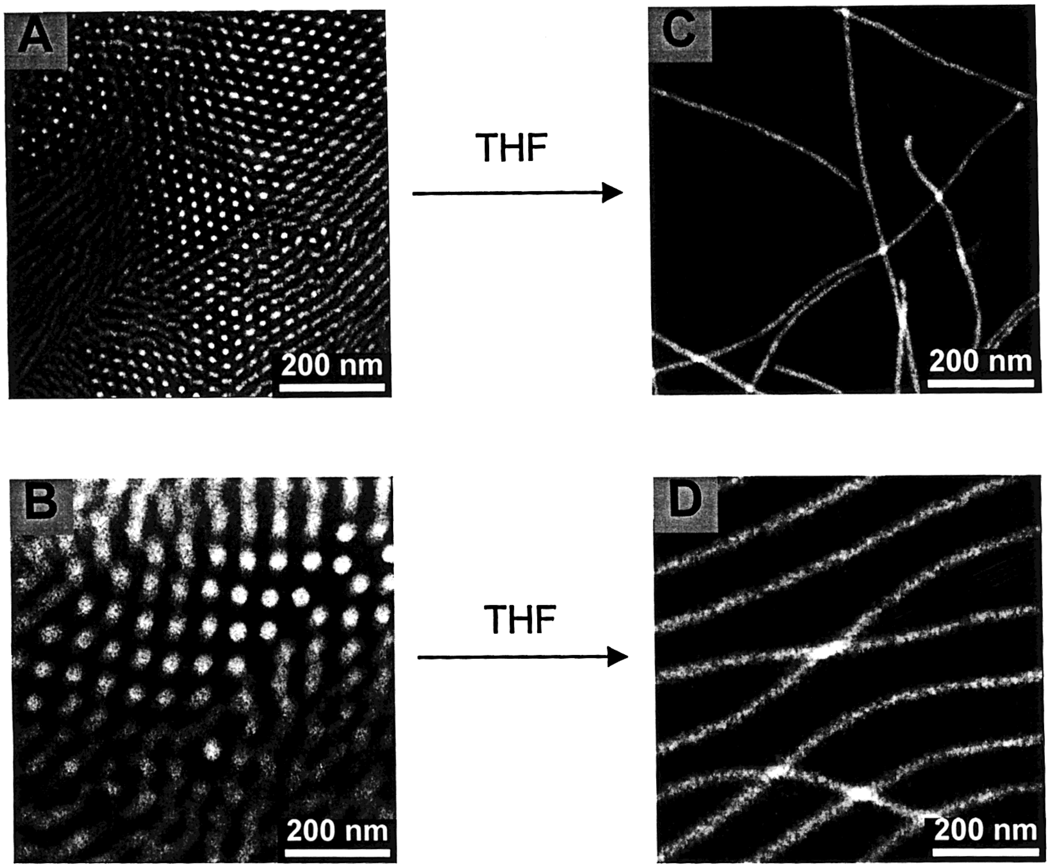

Figure 16. TEM micrographs of hybrid materials (A) PP5/2 (M_n(block) = 1.4 × 10^4 g/mol; w_{INORG} = 0.32) and (B) PP0/3 (M_n(block) = 8.4 × 10^4 g/mol; w_{INORG} = 0.28) and of the isolated nano-cylinders (C) and (D) obtained by dissolution in THF. This demonstrated the influence of the molecular weight of the block copolymer on the diameter of the cylinders that increases from 12.5 nm in (C) to 35 nm in (D).

as "hairy objects", analogous to the concept introduced in polymer science about 10 years ago for rodlike macromolecules.[147–149] Furthermore, the spheres in Figure 13A can be regarded as an extension of the core–shell concept[150,151] to organic–inorganic hybrid materials. Of interest from an application point of view is the use of the "hairy cylinders" or plates for reinforcement of polymers.[152,153] The advantage of these materials over conventionally used layered silicates is their intrinsic compatibility with the organic matrix.

Control over the synthesis and shape, i.e., tailoring of properties of these nano-objects, is tremendous. Increasing the weight fraction of inorganic material, w_{INORG}, with respect to the same PI-*b*-PEO block copolymer PP5 from $w_{INORG} = 0.28$ (PP5/6) to $w_{INORG} = 0.32$ (PP5/2) increases the cylinder diameter from ≈10 to 12.5 nm (Figure 15).

The use of block copolymers of different molecular weights at a given weight fraction, w_{INORG}, further extends the size control. As depicted in Figure 16, the diameter of the cylinders can be varied from ≈12.5 nm (PP5/2) to 35 nm (PP0/3) by increasing the molecular weight of the PI-*b*-PEO block copolymers from $M = 1.4 \times 10^4$ to $M = 8.4 \times 10^4$ g/mol.[142]

Nano-objects prepared from the hybrid bulk materials by the selective swelling of the PI block can be regarded as a one-, two-, or three-dimensional preceramic network.[154] Consequently, heat treatment should transform the networks into ceramic materials with a defined geometry. The loss of the organic components, followed by thermogravimetry and confirmed by thermal analysis,[54] results in shrinkage of the aluminosilicate phase. A comparison of the TEM micrographs of the cylindrical sample PP5/2 shows a decrease of the diameter from ≈12.5 nm before (Figure 15A) to 8.5 nm after calcinations (Figure 15C). A micrograph of the same material at lower magnification is depicted in Figure 17. It demonstrates that the ceramic objects extended over several micrometers and shows areas displaying high curvature and even loops. These arrangements must have been formed upon deposition of more flexible hairy rods before thermal treatment.

Hence, not only the connectivity of the objects but also their arrangement survive processing, opening access to nanoengineering of ceramic materials through the sequence of synthesis–dissolution manipulation–hardening.

5.2. Pathways to Possible Applications in Nanobiotechnology. Due to their nanosize and chemical inertness, these kinds of nano-objects are valuable candidates, for example, as markers or labels for sensor applications in the field of nanobiotechnology. The sol–gel technique has proven to be especially suited for preparing inorganic oxide thin films with functional organic molecules and organometallic complexes entrapped in the inorganic matrix.[155–157] Doped nano-objects can thus be yielded if the sol–gel process is performed in the presence of a structure-directing block copolymer *and*, for example, a dye. Among suitable dye molecules, ruthenium complexes are of particular inter-

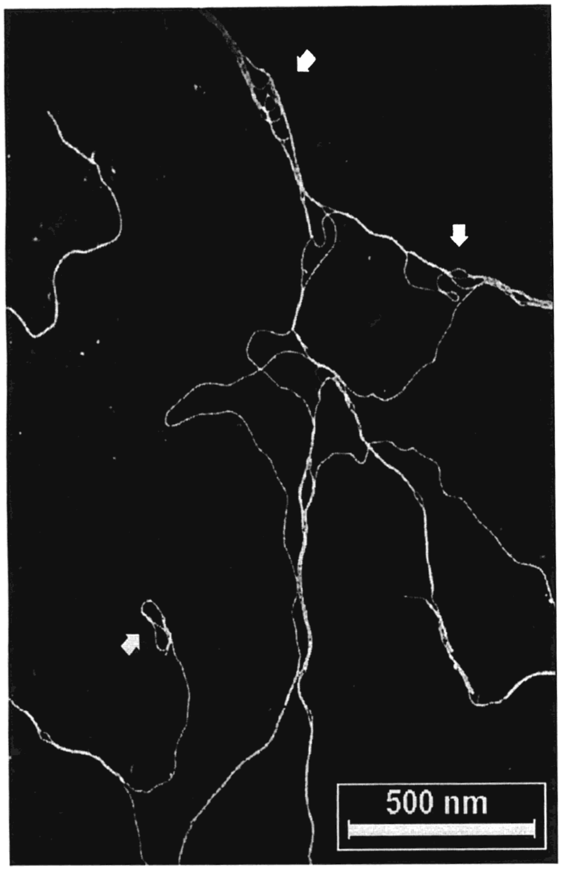

Figure 17. TEM micrograph of ceramic nanocylinders obtained by dissolution and heat treatment of PP5/2 (cf. Figure 15C). Arrows indicate regions of high curvature.

est. These complexes exhibit a variety of attractive functions based on luminescence properties with a long excited-state lifetime, redox properties, and excited-state reactivities combined with a relatively high chemical and thermal stability. So far, ruthenium complexes were successfully incorporated in inorganic oxide thin films[155,158,159] as well as in oxide bulk gels,[160,161] and applications in devices such as optical sensors have been demonstrated.[159,162]

In a straightforward approach, Ulrich[142] prepared nanocylinders by addition of tris(2,2′-bipyridyl)ruthenium(II) to a prehydrolyzed GLYMO−Al(O^{s}Bu)$_3$ solution in the presence of PI-*b*-PEO as a structure-directing agent and subsequent dissolution of bulk material. TEM micrographs of the resulting structures are shown in Figure 18. The presence of the organometallic dye did not interfere with the sol−gel process. Because bleaching was not observed even after dialysis of the isolated nanocylinders, it can be concluded that the fluorescent dye molecules are firmly entrapped in the aluminosilicate matrix. This strategy paves the way to fluorescent spheres, cylinders, and plates with dimensions of 10−50 nm. Furthermore, the “hairy” surface of these objects allows a fine-tuning of their solution properties by chemical modifications.

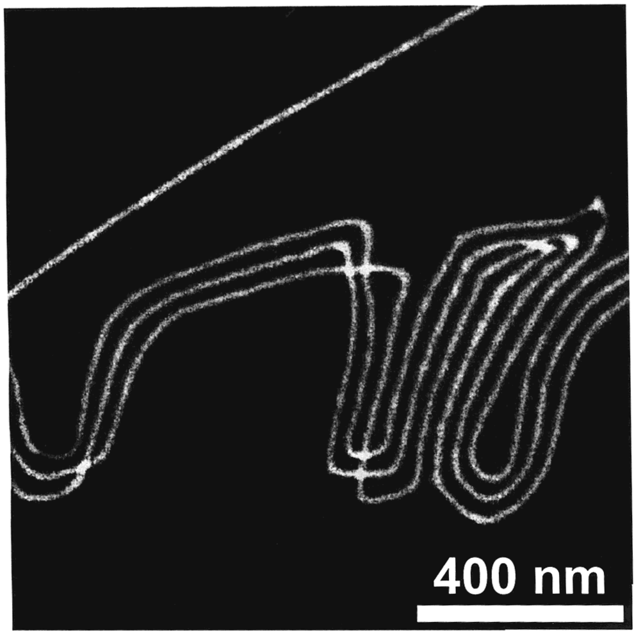

Figure 18. TEM micrograph of fluorescent cylinders prepared by addition of tris(2,2′-bipyridyl)ruthenium(II) to a prehydrolyzed GLYMO−Al(O^{s}Bu)$_3$ solution in the presence of PI-*b*-PEO.

For certain sensor applications a length of the nanocylinders shorter than micrometers may be desirable. This can be achieved by treating them with ultrasound. A TEM micrograph showing nanocylinders with an average length of about 200 nm obtained after such a treatment is depicted in Figure 19 (compare with micrometer length cylinders in Figure 17).[142] Thus, besides composition and diameter, the length of nanocylinders can conveniently be adjusted to specific needs as well.

5.3. Preparation of Mesoporous Materials. The synthesis of nano-, meso-, and microporous silicate materials using the structure-directing properties of organic molecules is an area of rapid growth with diverse applications, such as separation technology and catalysis. Zeoliths, although appearing in nature,[163,164] can be prepared by application of organic molecules, e.g., tertiary amines.[165] They exhibit a periodical pattern of cavities connected by channels. The synthesis of mesoporous M41S zeoliths was first achieved using amphiphilic molecules with long hydrophobic chains as structure-directing agents.[77] In this case aggregates rather than single molecules are responsible for the structure-directing effect leading to, e.g., MCM41 with hexagonal and MCM48 with a cubic pore pattern.[125,166−169] Their potential in catalysis, as templates[170] and in separation technology, was outlined in recent publications.[16,171−173]

Use of block copolymers has recently been shown to extend the pore sizes of ordered porous silica to hundreds of Angstroms.[53,82,172,174] Combined principles of polymer, colloidal, and inorganic chemistries have been used to synthesize materials with uniform and adjustable pore sizes and with thick, hydrothermally stable walls.[175] Both two-dimensional (2D) hexagonal structures and three-dimensional (3D) cubic morphologies with more accessible pores have been synthesized. The synthesis strategy has been generalized to various metal oxides and hierarchical oxide structures.[175−177]

In the preceding sections it was shown that the preparation of an inverse cylindrical as well as a bicontinuous cubic structure could be achieved by employing PI-*b*-PEO as structure-directing agents. For such structures with PI in the minority phase, embedded in the majority phase of the aluminosilicate/PEO

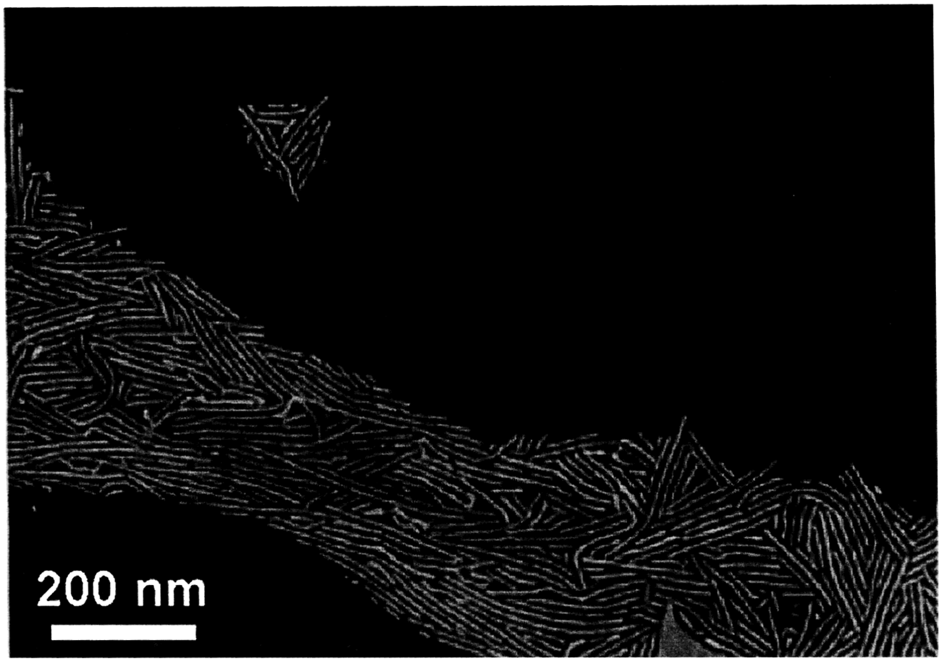

Figure 19. TEM micrograph of a monolayer of cylinders on a carbon surface. The monolayer film was obtained by ultrasound treatment of a diluted solution of nanocylinders in chloroform and casting of this solution on a water surface.

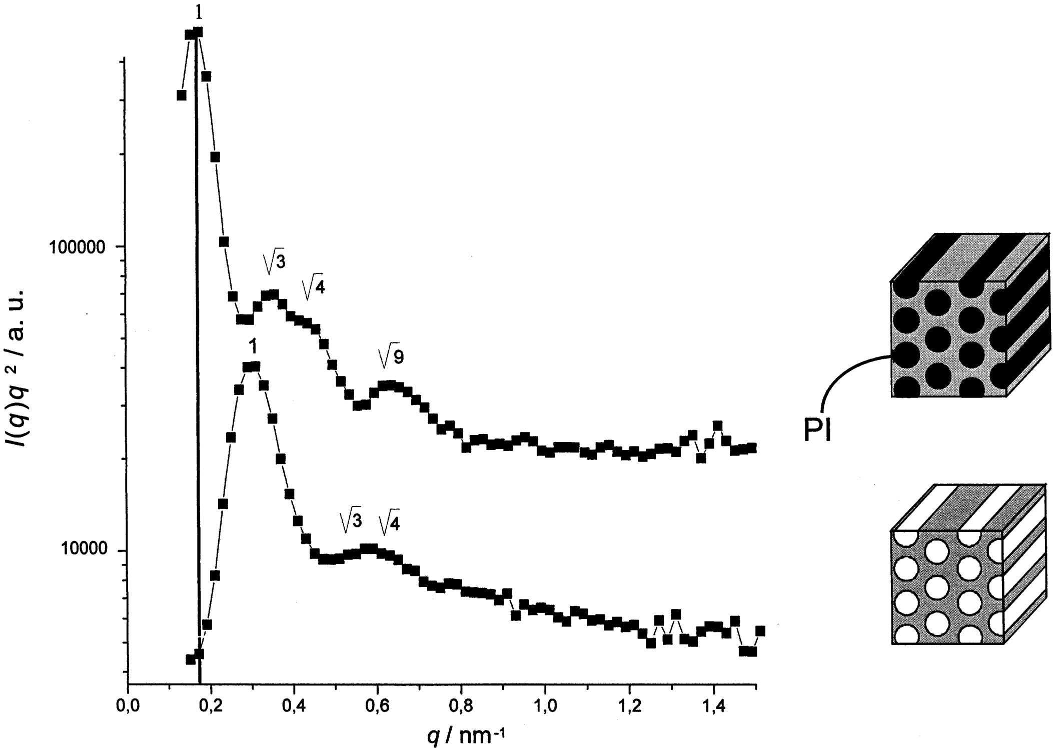

Figure 20. SAXS data of the hexagonal packed hybrid material PP5/4 before (top) and after (bottom) calcination. Angular positions of higher order peaks with respect to the first-order maximum are indicated for each curve.

network, heat treatment at elevated temperatures is expected to lead to mesoporous materials with accessible pores as sketched in Scheme 9.

The preparation of these kinds of materials has indeed recently been reported by Ulrich[142] and Finnefrock et al.[144] They used nanocomposites with an inverse cylindrical and a plumber's nightmare (cf. Figure 12B) morphology, respectively, which after heat treatment in several stages up to 600 °C were converted successfully to the corresponding mesoporous materials.

Representative SAXS data of a sample with inverse hexagonal morphology before and after calcinations are shown in Figure 20. Most evident is the significant shift of the first-order peak of the calcined material toward a larger scattering vector, *q*. In fact, the average distance between two cylinders is reduced through heat treatment down to 62% of its original value. This goes along with a mass loss of about 75%! Despite this large shrinkage and mass loss, which is due to the large fraction of organic moieties even in the inorganic phase

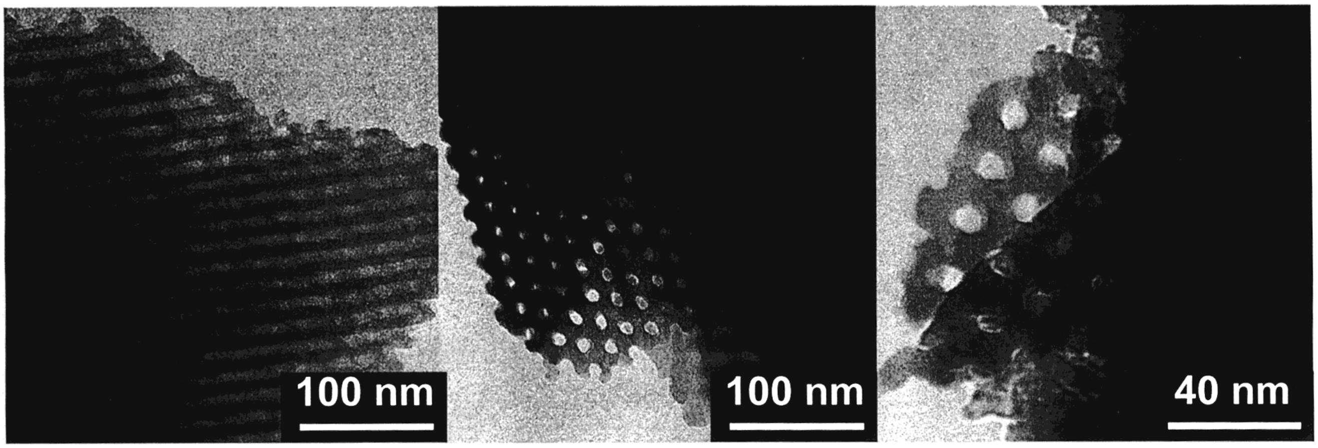

Figure 21. Bright field transmission electron microscopy (TEM) data of the hexagonal packed sample PP5/2 after calcinations. Bright areas correspond to the voids.

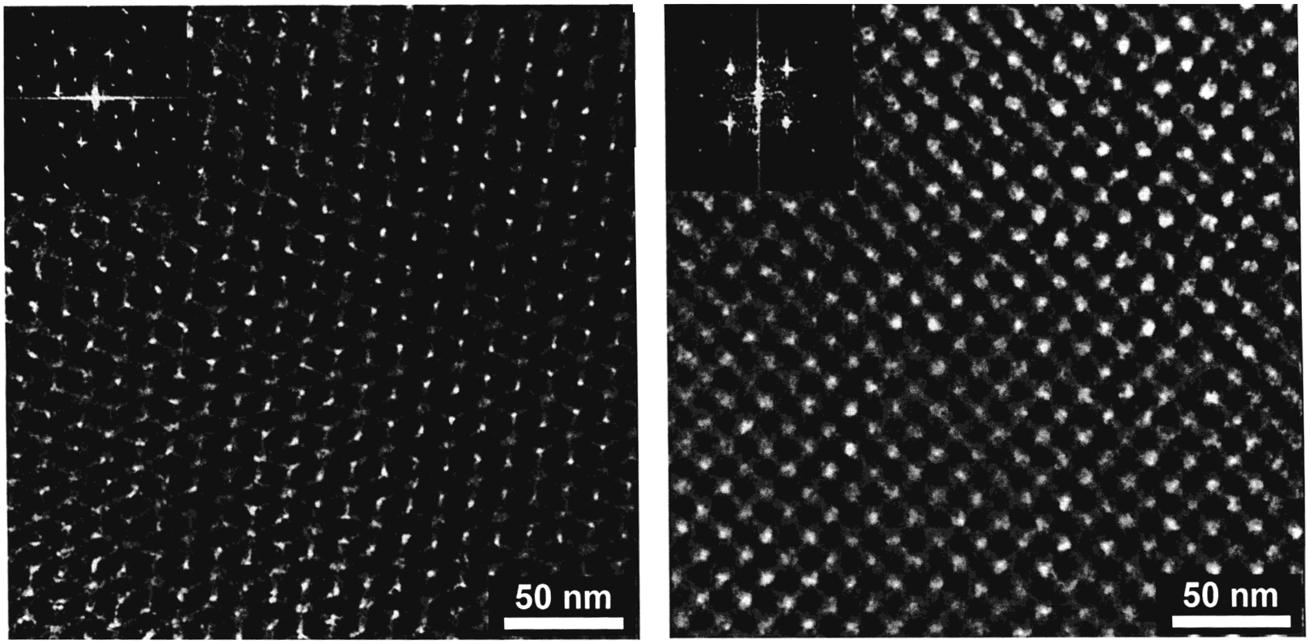

Figure 22. Bright field transmission electron microscopy (TEM) from calcined material highlighting the 3-fold (left) and the 4-fold (right) projections of the cubic phase. Insets to each panel show the computed Fourier diffraction patterns.

of the hybrid, the SAXS data of the calcined materials show higher order reflections consistent with a hexagonal long-range order. This result is corroborated by the TEM results depicted in Figure 21, clearly demonstrating the hexagonal symmetry of the calcined sample. From these TEM data the average distance between the centers of two cylinders is about 22.5 nm, which is in good agreement with the SAXS results of 24 nm. The pore diameter from TEM is about 10.5 nm.

Bright-field transmission electron microscopy (TEM) data on a calcined sample of the plumber's nightmare material are shown in Figure 22. Bright areas correspond here to the voids, while dark areas correspond to the ceramic phase. It is easy to identify thin, *connected* volumes (channels) with 4-fold and 3-fold ("wagon-wheel") orientations, typical of a bicontinuous cubic structure.

The TEM data together with the analysis of the corresponding SAXS data shown in Figure 23 suggest a "Plumber's Nightmare" structure also for the calcined sample. Although somewhat lower than in the as-made sample (Figure 12), the degree of order of this sample is still remarkably high. Consistent with the large grain sizes observed by electron microscopy, the distinct peaks in the SAXS image again imply that the X-ray beam (<0.1 mm^2) averages only over a limited number of crystallites with different orientations. Analysis of the SAXS data indeed shows that peaks originate from only six microdomains within the calcined sample.

As in the case of the as-made sample, the SAXS data are consistent with $Im\bar{3}m$ symmetry, and the lattice basis length can be determined to be 395 Å for the calcined sample, consistent with the analysis of the TEM data.

It is striking that the symmetry is so well-preserved after calcination, even though the lattice constant falls to ≈60% of its uncalcined value (the cell volume falls to about 25%!). This indicates that the bonding network formed by the inorganic precursors is extremely robust. This may be a general feature of the present block copolymer derived hybrid materials. After calcination the bulk material consists of an aluminosilicate matrix

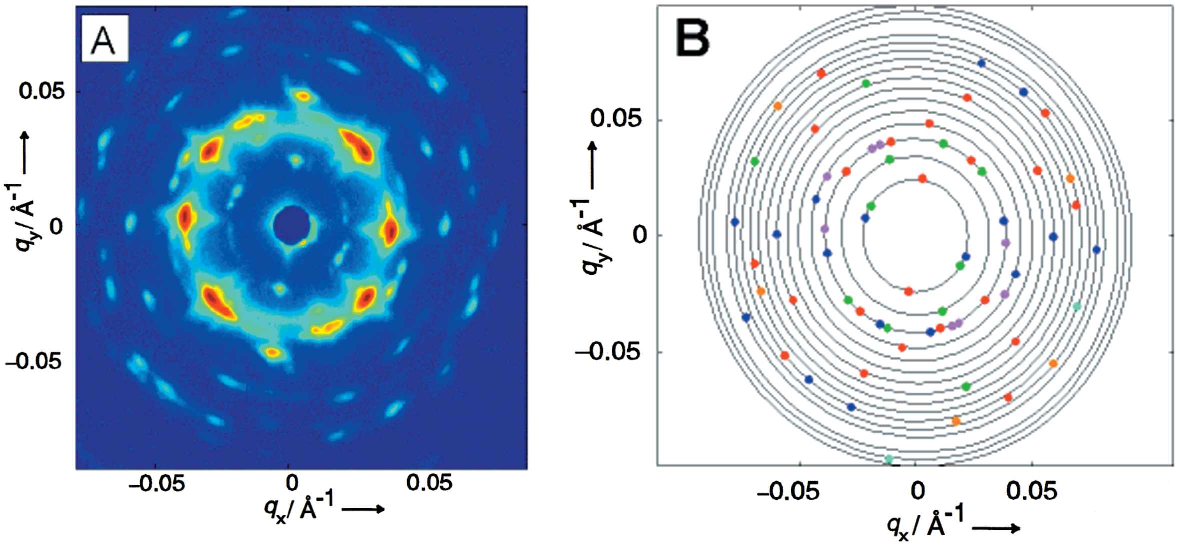

Figure 23. (A) SAXS image and (B) indexed peak positions for the calcined sample. For specifics, see Figure 12.

Scheme 10. Complexity Diagram for Blocked Macromolecules

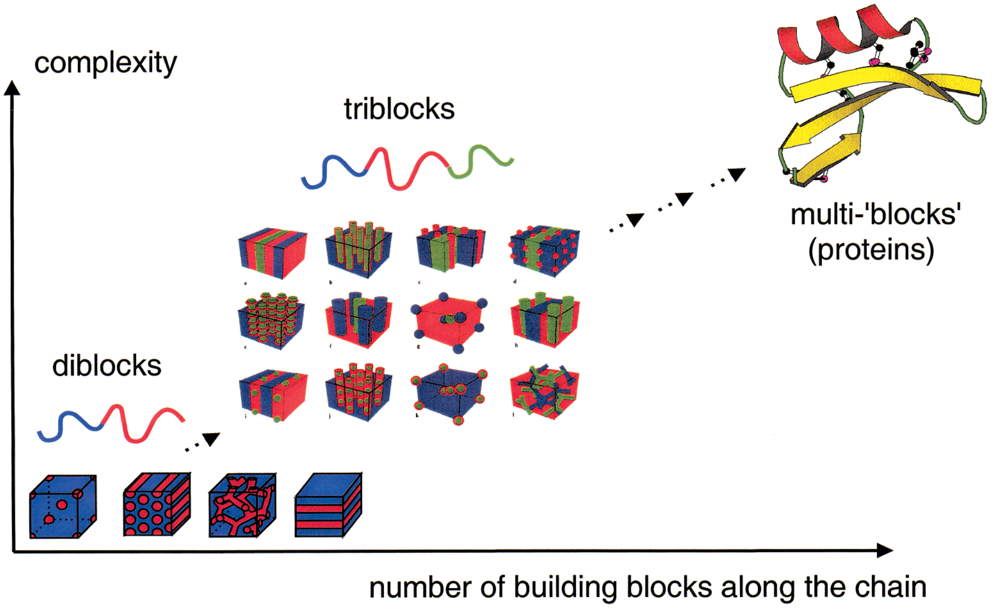

interwoven with two discrete, continuous nanochannel systems that do not touch each other (see Scheme 8B). The important question about the accessibility of the pores in both hexagonal and plumber's nightmare materials could be resolved through measurements of the corresponding nitrogen sorption isotherms.[142,144]

Both mesoporous materials exhibit a nitrogen sorption isotherm of type IV according to BDDT classification with a specific surface area of 300 m^2/g for the plumber's nightmare and 280 m^2/g for the hexagonal material according to the Brunnauer–Emmett–Teller (BET) method.[178] The lower specific surface area as compared to pure SiO_x materials with comparable pore sizes, which ranges from 630 to 850 m^2/g,[172] is caused by the higher density of the present aluminosilicate. Aluminosilicates comparable to the present materials[177] indeed exhibit an almost identical surface area (300–350 m^2/g).

Calculation of the pore size distribution from the desorption branch of the isotherm reveals in both cases a slightly bimodal pore size distribution with an average pore diameter according to BJH (Barrett–Joyner–Halenda)[179] of ≈9 nm. The specific pore volume can be calculated following the Gurvitch rule[180] to be 0.47 mL/g (plumber's nightmare) and 0.50 mL/g (hexagonal), respectively.

That specific surface areas and pore sizes are so similar for both materials is due to the similar weight fraction of the PEO/GLYMO/Al(O^sBu)$_3$ phase in both materials (≈22 wt % PI for hexagonal sample and ≈27 wt % PI for the bicontinuous cubic sample). They only significantly differ in their PEO fraction, which determined the morphology, however, as discussed in section 4.

It is interesting to note that, in the present hexagonal mesoporous material with about 12 nm, the wall thickness is about twice as large as that of materials described in the literature.[172,177] This should lead to significantly improved stability. Furthermore, the pore sizes of the present materials can be varied through a simple variation of the molecular weight of the precursor PI-*b*-PEO obtained through anionic polymerization. As an example, from the PI-*b*-PEO sample PP0 with $M_n = 8.4 \times 10^4$, $f_{PEO} \approx 0.08$, and polydispersity, $M_w/M_n = 1.05$, a hybrid material with inverse hexagonal morphology was prepared at $w_{INORG} = 0.28$ and then calcined. Analysis of the corresponding nitrogen sorption isotherm revealed a pore size of about 50 nm.[142]

6. Conclusion and Outlook

The study of amphiphilic polymer based polymer−ceramic hybrid materials is an exciting emerging research area offering enormous scientific and technological promise. By choice of the appropriate block copolymer system (PI-*b*-PEO) as well as ceramic precursors (ormocers), unprecedented morphology control on the nanoscale is obtained. It is based on a unique polymer−ceramic interface that was characterized in detail by solid-state NMR measurements. The hydrophilic parts of the block copolymers are completely integrated into the ceramic phase, analogous to what is often found in biological hybrid materials. The resulting composites can be described as a "quasi two-phase system", allowing for a more rational hybrid morphology design based on the current understanding of the phase behavior of block copolymers and copolymer−homopolymer mixtures. The structures generated on the nanoscale are a result of a fine balance of competing interactions, another feature of complex biological systems. In the present contribution the synthesis and characterization of nanostructured hybrids based on aluminosilicates has been described, spanning the entire phase space of block copolymers. Besides morphologies known from other polymer studies, the existence of a "plumber's nightmare" phase was suggested. This indicates subtle, not yet understood differences from conventional block copolymer systems. Nanoengineering of such hybrids toward applications has been demonstrated in the area of nano-objects of predetermined size, shape, and composition for nanobiotechnology as well as mesoporous materials for separation technology and catalysis.

The future potential of this approach for new materials lies in the versatility of the polymer chemistry as well as that of the sol−gel chemistry that can be exploited in the materials synthesis. Focusing on the polymer side, Scheme 10, shows a complexity diagram for blocked (compartmented) macromolecules.[181] It illustrates that when the number of building blocks along the chain is increased, the complexity of the resulting structures is elevated significantly. For the case of passing from AB diblock copolymers to ABC triblock copolymers, this has already been demonstrated.[182−187] A whole range of new morphologies has been found for ABC triblocks and to understand their phase behavior in detail is a current area of intensive research. It constitues an interesting challenge to try to use those polymer systems as structure-directing agents for the generation of nanostructured polymer−inorganic hybrid materials. In this way, e.g., inorganic nano-objects in the form of rings or even helices should become accessible. This is only one possible future pathway research could go along, however, since the variety of the polymer chemistry as well as that of the inorganic sol−gel chemistry is only limited by one's imagination (cf. Scheme 10).

Acknowledgment. This review is based on several years of research on block copolymer−ormocer hybrid materials started at the Max-Planck Institute for Polymer Research in Mainz and now continued at Cornell University in Ithaca. It is our pleasure to thank the following co-workers that were engaged in this research: M. Templin, A. Du Chesne, S. De Paul, V. Schädler, Y. Zhang, H. Leist, U. Friedrich, C. Honeker, and A. Franck. Our work benefited from fruitful collaborations with K. Schumacher and K. Unger, Mainz University, J. Zwanziger, Indiana University, G. Floudas, F.O.R.T.H, and A. Finnefrock and S. Gruner, Cornell University. The financial support of the Max-Planck-Society and the National Science Foundation (Grant DMR-0072009) is gratefully acknowledged. The work was further supported by the Cornell Center for Materials Research (CCMR), a Materials Research Science and Engineering Center of the National Science Foundation (DMR-0079992).

References

(1) Weiss, A. *Angew. Chem., Int. Ed. Engl.* **1981**, *20*, 850.
(2) Krampitz, G.; Witt, W. *Top. Curr. Chem.* **1979**, *78*, 57.
(3) Sarikaya, M.; Aksay, I. A. *Biomimetics: Design and Processing of Materials*; AIP Press: Woodbury, N.Y., 1995.
(4) Mann, S.; Ozin, G. A. *Nature* **1996**, *382*, 313.
(5) Lehn, J.-M. *Angew. Chem., Int. Ed. Engl.* **1988**, *27*, 89.
(6) Ringsdorf, H.; Schlarb, B.; Venzmer, J. *Angew. Chem., Int. Ed. Engl.* **1988**, *27*, 113.
(7) Ahlers, M.; Müller, W.; Reichert, A.; Ringsdorf, H.; Venzmer, J. *Angew. Chem., Int. Ed. Engl.* **1990**, *29*, 1269.
(8) Bates, F. S. *Science* **1991**, *251*, 898.
(9) Heuer, A. H.; Fink, D. J.; Laraia, V. J.; Arias, J. L.; Calvert, P. D.; Kendall, K.; Messing, G. L.; Blackwell, J.; Rieke, P. C.; Thompson, D. H.; Wheeler, A. P.; Veis, A.; Caplan, A. I. *Science* **1992**, *255*, 1098.
(10) Mann, S.; Archibald, D. D.; Didymus, J. M.; Douglas, T.; Heywood, B. R.; Meldrum, F. C.; Reeves, N. J. *Science* **1993**, *261*, 1286.
(11) Huo, Q.; Margolese, D. I.; Ciesla, U.; Feng, P.; Gier, T. E.; Sieger, P.; Leon, R.; Petroff, P. M.; Schüth, F.; Stucky, G. D. *Nature* **1994**, *368*, 317.
(12) Aksay, I. A.; Trau, M.; Manne, S.; Honma, I.; Yao, N.; Zhou, L.; Fenter, P.; Eisenberger, P. M.; Gruner, S. M. *Science* **1996**, *273*, 892.
(13) Osenar, P.; Braun, P. V.; Stupp, S. I. *Adv. Mater.* **1996**, *8*, 1022.
(14) Braun, P. V.; Osenar, P.; Stupp, S. I. *Nature* **1996**, *380*, 325.
(15) Mann, S.; Burkett, S. L.; Davis, S. A.; Fowler, C. E.; Mendelson, N. H.; Sims, S. D.; Walsh, D.; Whilton, N. T. *Chem. Mater.* **1997**, *9*, 2300.
(16) Antonietti, M.; Göltner, C. *Angew. Chem., Int. Ed. Engl.* **1997**, *36*, 911.
(17) Percec, V.; Ahn, C.-H.; Ungar, G.; Yeardley, D. J. P.; Möller, M.; Sheiko, S. S. *Nature* **1998**, *391*, 161.
(18) Luzzati, V.; Mustacchi, H.; Skoulios, A.; Husson, F. *Acta Crystallogr.* **1960**, *13*, 660.
(19) Seddon, J.; Templer, R. *New Scientist* **1991**, *1769*, 45.
(20) Fendler, J. H. *Adv. Polym. Sci.* **1994**, *113*, 1.
(21) Chiruvolu, S.; Walker, S. A.; Israelachvili, J. N.; Schmitt, F. J.; Leckband, D.; Zasadzinski, J. A. *Science* **1994**, *264*, 1753.
(22) Spector, M. S.; Zasadzinski, J. A.; Sankaram, M. B. *Langmuir* **1996**, *12*, 4704.
(23) Schnur, J. M. *Science* **1993**, *262*, 1669.
(24) Schnur, J. M.; Ratna, B. R.; Selinger, J. V.; Singh, A.; Jyothi, G.; Easwaran, K. R. K. *Science* **1994**, *264*, 945.
(25) Thomas, B. N.; Safinya, C. R.; Plano, R. J.; Clark, N. A. *Science* **1995**, *1995*, 1635.
(26) Hillmyer, M. A.; Bates, F. S.; Almdal, K.; Mortensen, K.; Ryan, A. J.; Fairclough, J. P. A. *Science* **1996**, *271*, 976.
(27) Mendes, E.; Schädler, V.; Marques, C. M.; Lindner, P.; Wiesner, U. *Europhys. Lett.* **1997**, *40*, 521.
(28) Mendes, E.; Wiesner, U.; Schaedler, V.; Lindner, P. *Prog. Colloid Polym. Sci.* **1832**, *110*, 220.
(29) Schädler, V.; Lindner, P.; Wiesner, U.; Mendes, E. *J. Phys. Chem. B* **1998**, *102*, 7316.
(30) Schädler, V.; Nardin, C.; Wiesner, U.; Mendes, E. *J. Phys. Chem. B* **2000**, *104*, 5049.
(31) Price, C. *Pure Appl. Chem.* **1983**, *55*, 1563.
(32) Singh, A.; Schoen, P. E.; Schnur, J. M. *J. Chem. Soc., Chem. Commun.* **1988**, 1222.

(33) Antonietti, M.; Heinz, S.; Schmidt, M.; Rosenauer, C. *Macromolecules* **1994**, *27*, 3276.
(34) Zhang, L.; Eisenberg, A. *Science* **1995**, *268*, 1728.
(35) Spatz, J. P.; Mössmer, S.; Möller, M. *Angew. Chem., Int. Ed. Engl.* **1996**, *35*, 1510.
(36) Zhang, L.; Eisenberg, A. *J. Am. Chem. Soc.* **1996**, *118*, 3168.
(37) Liu, G. *Adv. Mater.* **1997**, *9*, 437.
(38) Ding, J.; Liu, G. *Chem. Mater.* **1998**, *10*, 537.
(39) Yu, K.; Eisenberg, A. *Macromolecules* **1998**, *31*, 3509.
(40) Yu, K.; Bartels, C.; Eisenberg, A. *Langmuir* **1999**, *15*, 7157.
(41) Alexandridis, P.; Spontak, R. J. *Curr. Opin. Colloid Interface Sci.* **1999**, *4*, 130.
(42) Halperin, A.; Tirrell, M.; Lodge, T. P. *Adv. Polym. Sci.* **1992**, *100*, 31.
(43) Förster, S.; Zisenis, M.; Wenz, E.; Antonietti, M. *J. Chem. Phys.* **1996**, *104*, 9956.
(44) Yu, K.; Zhang, L.; Eisenberg, A. *Langmuir* **1996**, *12*, 5980.
(45) Yu, K.; Eisenberg, A. *Macromolecules* **1996**, *29*, 6359.
(46) Yu, Y.; Eisenberg, A. *J. Am. Chem. Soc.* **1997**, *119*, 8383.
(47) Förster, S.; Antonietti, M. *Adv. Mater.* **1998**, *10*, 195.
(48) Desbaumes, L.; Eisenberg, A. *Langmuir* **1999**, *15*, 36.
(49) Pepin, M. P.; Whitmore, M. D. *Macromolecules* **2000**, *33*, 8644.
(50) Hamley, I. W. *The Physics of Block Copolymers*; Oxford University Press: Oxford, 1998.
(51) Schubert, U.; Hüsing, N.; Lorenz, A. *Chem. Mater.* **1995**, *7*, 2010.
(52) Judeinstein, P.; Sanchez, C. *J. Mater. Chem.* **1996**, *6*, 511.
(53) Templin, M.; Franck, A.; Du Chesne, A.; Leist, H.; Zhang, Y.; Ulrich, R.; Schädler, V.; Wiesner, U. *Science* **1997**, *278*, 1795.
(54) Ulrich, R.; Du Chesne, A.; Templin, M.; Wiesner, U. *Adv. Mater.* **1999**, *11*, 141.
(55) Mackenzie, J. D. *ACS Symp. Ser.* **1995**, *585*, 226.
(56) Schmidt, H. *J. Non-Cryst. Solids* **1985**, *73*, 681.
(57) Ravaine, D.; Seminel, A.; Charbouillot, Y.; Vincens, M. *J. Non-Cryst. Solids* **1986**, *82*, 210.
(58) Wen, J.; Wilkes, G. L. *Chem. Mater.* **1996**, *8*, 1667.
(59) Brinker, J. C.; Scherer, G. W. *Sol−Gel Science: The Physics and Chemistry of Sol−Gel Processing*; Academic Press: Boston, 1990.
(60) Yoldas, B. E. *J. Mater. Sci.* **1979**, *14*, 1843.
(61) Fyfe, C. A.; Aroca, P. P. *Chem. Mater.* **1995**, *7*, 1800.
(62) Corriu, R. J. P.; Leclercq, D. *Angew. Chem., Int. Ed. Engl.* **1996**, *35*, 1421.
(63) Yoldas, B. E. *J. Mater. Sci.* **1986**, *21*, 1087.
(64) Templin, M.; Wiesner, U.; Spiess, H. W. *Adv. Mater.* **1997**, *9*, 814.
(65) Engelhardt, G.; Michel, D. *High-Resolution Solid-State NMR of Silicates and Zeolites*; J. Wiley: Chichester, New York, 1987.
(66) Babonneau, F. *Mater. Res. Soc. Symp. Proc.* **1994**, *346*, 949.
(67) Schmidt-Rohr, K.; Spiess, H. M. *Multidimensional Solid-State NMR and Polymers*; Academic Press: London, San Diego, 1994.
(68) Peeters, M. P. J.; Wakelkamp, W. J. J.; Kentgens, A. P. M. *J. Non-Cryst. Solids* **1995**, *189*, 77.
(69) Spiess, H. W. *Ber. Bunsen-Ges. Phys. Chem.* **1997**, *101*, 153.
(70) Hartmann, S. R.; Hahn, E. L. *Phys. Rev.* **1962**, *128*, 2042.
(71) Innocenzi, P.; Brusatin, G.; Babonneau, F. *Chem. Mater.* **2000**, *12*, 3726−3732.
(72) Müller, D.; Gessner, W.; Behrens, H. J.; Scheler, G. *Chem. Phys. Lett.* **1981**, *79*, 59.
(73) Lippmaa, E.; Mägi, M.; Samoson, A.; Engelhardt, G.; Grimmer, A. R. *J. Am. Chem. Soc.* **1980**, *102*, 4889.
(74) Chmelka, B. F.; Pines, A. *Science* **1989**, *246*, 71.
(75) Templin, M.; Friedrich, U.; Wiesner, U.; Spiess, H. W. In *Precursor-Derived Ceramics*; Bill, J., Wakai, F., Aldinger, F., Eds.; Wiley-VCH: Weinheim, 1999; p 205.
(76) Irwin, A. D.; Holmgren, J. S.; Jonas, J. *J. Mater. Sci.* **1988**, *23*, 2908.
(77) Kresge, C. T.; Leonowicz, M. E.; Roth, W. J.; Vartuli, J. C.; Beck, J. S. *Nature* **1992**, *359*, 710.
(78) Raman, N. K.; Anderson, M. T.; Brinker, C. J. *Chem. Mater.* **1996**, *8*, 1682.
(79) Huo, Q.; Leon, R.; Petroff, P. M.; Stucky, G. D. *Science* **1995**, *268*, 1324.
(80) Firouzi, A.; Kumar, D.; Bull, L. M.; Besier, T.; Sieger, P.; Huo, Q.; Walker, S. A.; Zasadzinski, J. A.; Glinka, C. *Science* **1995**, *267*, 1138.
(81) Huo, Q.; Margolese, D.; Stucky, G. D. *Chem. Mater.* **1996**, *8*, 1147.
(82) Bagshaw, S. A.; Prouzet, E.; Pinnavaia, T. J. *Science* **1995**, *269*, 1242.
(83) Attard, G. S.; Glyde, J. C.; Göltner, C. G. *Nature* **1995**, *378*, 366.
(84) Firouzi, A.; Atef, F.; Oertli, A. G.; Stucky, G. D.; Chmelka, B. F. *J. Am. Chem. Soc.* **1997**, *119*, 3596.
(85) Sankaran, V.; Cummins, C. C.; Schrock, R. R.; Cohen, R. E.; Silbey, R. J. *J. Am. Chem. Soc.* **1990**, *112*, 6858.
(86) Chan, Y. N. C.; Schrock, R. R.; Cohen, R. E. *Chem. Mater.* **1992**, *4*, 24.
(87) Moffitt, M.; McMahon, L.; Pessel, V.; Eisenberg, A. *Chem. Mater.* **1995**, *7*, 1185.
(88) Spatz, J. P.; Roescher, A.; Sheiko, S.; Krausch, G.; Moeller, M. *Adv. Mater.* **1995**, *7*, 731.
(89) Antonietti, M.; Wenz, E.; Bronstein, L.; Seregina, M. *Adv. Mater.* **1995**, *7*, 1000.
(90) Clay, R. T.; Cohen, R. E. *Supramol. Sci.* **1996**, *2*, 183.
(91) Kane, R. S.; Cohen, R. E.; Silbey, R. J. *Chem. Mater.* **1996**, *8*, 1919.
(92) Raez, J.; Barjovanu, R.; Massey, J. A.; Winnik, M. A.; Manners, I. *Angew. Chem., Int. Ed.* **2000**, *39*, 3862.
(93) Rulkens, R.; Ni, Y.; Manners, I. *J. Am. Chem. Soc.* **1994**, *116*, 12121.
(94) Ni, Y.; Rulkens, R.; Manners, I. *J. Am. Chem. Soc.* **1996**, *118*, 4102.
(95) Massey, J.; Power, K. N.; Manners, I.; Winnik, M. A. *J. Am. Chem. Soc.* **1998**, *120*, 9533.
(96) Massey, J. A.; Power, K. N.; Winnik, M. A.; Manners, I. *Adv. Mater.* **1998**, *10*, 1559.
(97) Manners, I. *Pure Appl. Chem.* **1998**, *71*, 1471.
(98) Bates, F. S.; Fredrickson, G. H. *Phys. Today* **1999**, *52*, 32.
(99) Leibler, L. *Macromolecules* **1980**, *13*, 1602.
(100) Förster, S.; Khandpur, A. K.; Zhao, J.; Bates, F. S.; Hamley, I. W.; Ryan, A. J.; Bras, W. *Macromolecules* **1994**, *27*, 6922.
(101) Hajduk, D. A.; Takenouchi, H.; Hillmyer, M. A.; Bates, F. S.; Vigild, M. E.; Almdal, K. *Macromolecules* **1997**, *30*, 3788.
(102) Vigild, M. E.; Almdal, K.; Mortensen, K.; Hamley, I. W.; Fairclough, J. P. A.; Ryan, A. J. *Macromolecules* **1998**, *31*, 5702.
(103) Hajduk, D. A.; Harper, P. E.; Gruner, S. M.; Honeker, C. C.; Kim, G.; Thomas, E. L.; Fetters, L. J. *Macromolecules* **1994**, *27*, 4063.
(104) Olvera de la Cruz, M.; Sanchez, I. C. *Macromolecules* **1986**, *19*, 2501.
(105) Floudas, G.; Hadjichristidis, N.; Iatrou, H.; Pakula, T.; Fischer, E. W. *Macromolecules* **1994**, *27*, 7735.
(106) Floudas, G.; Pispas, S.; Hadjichristidis, N.; Pakula, T.; Erukhimovich, I. *Macromolecules* **1996**, *29*, 4142.
(107) Floudas, G.; Hadjichristidis, N.; Tselikas, Y.; Erukhimovich, I. *Macromolecules* **1997**, *30*, 3090.
(108) Floudas, G.; Hadjichristidis, N.; Iatrou, H.; Avgeropoulos, A.; Pakula, T. *Macromolecules* **1998**, *31*, 6943.
(109) Fredrickson, G. H.; Helfand, E. *J. Chem. Phys.* **1987**, *87*, 697.
(110) Erukhimovich, I.; Dobrynin, A. V. *Macromol, Symp.* **1994**, *81*, 253.
(111) Vavasour, J. D.; Whitmore, M. D. *Macromolecules* **1993**, *26*, 7070.
(112) Vavasour, J. D.; Whitmore, M. D. *Macromolecules* **1996**, *29*, 5244.
(113) Matsen, M. W.; Schick, M. *Macromolecules* **1994**, *27*, 4014.
(114) Matsen, M. W.; Bates, F. S. *J. Polym. Sci., Part B: Polym. Phys.* **1997**, *35*, 945.
(115) Floudas, G.; Ulrich, R.; Wiesner, U. *J. Chem. Phys.* **1999**, *110*, 652.
(116) Floudas, G.; Ulrich, R.; Wiesner, U.; Chu, B. *Europhys. Lett.* **2000**, *50*, 182.
(117) Floudas, G.; Vazaiou, B.; Schipper, F.; Ulrich, R.; Wiesner, U.; Iatrou, H.; Hadjichristidis, N. *Macromolecules* **2001**, *34*, 2947.
(118) Du Chesne, A.; Lieser, G.; Wegner, G. *Colloid Polym. Sci.* **1994**, *272*, 1329.
(119) Du Chesne, A.; Wenke, K.; Lieser, G.; Wenz, G. *Acta Polym.* **1997**, *48*, 142.
(120) Du Chesne, A. *Macromol. Chem. Phys.* **1999**, *200*, 1813.
(121) Reimer, L. *Adv. Electron. Electron. Phys.* **1991**, *81*, 43.
(122) Hashimoto, T.; Nagatoshi, K.; Todo, A.; Hasegawa, H.; Kawai, H. *Macromolecules* **1974**, *7*, 364.
(123) Ehlich, D.; Takenaka, M.; Okamoto, S.; Hashimoto, T. *Macromolecules* **1993**, *26*, 189.
(124) Honeker, C. C.; Thomas, E. L. *Chem. Mater.* **1996**, *8*, 1702.
(125) Monnier, A.; Schüth, F.; Huo, Q.; Kumar, D.; Margolese, D.; Maxwell, R. S.; Stucky, G. D.; Krishnamurty, M.; Petroff, P. M.; Firouzi, A.; Janike, M.; Chmelka, B. F. *Science* **1993**, *261*, 1299.
(126) Hillmyer, M. A.; Lipic, P. M.; Hajduk, D. A.; Almdal, K.; Bates, F. S. *J. Am. Chem. Soc.* **1997**, *119*, 2749.
(127) Lipic, P. M.; Bates, F. S.; Hillmyer, M. A. *J. Am. Chem. Soc.* **1998**, *120*, 8963.
(128) Hashimoto, T.; Tanaka, H.; Hasegawa, H. *Macromolecules* **1990**, *23*, 4378.
(129) Tanaka, H.; Hasegawa, H.; Hashimoto, T. *Macromolecules* **1991**, *24*, 240.
(130) Shull, K. R.; Winey, K. I. *Macromolecules* **1992**, *25*, 2637.
(131) Matsen, M. W. *Macromolecules* **1995**, *28*, 5765.
(132) Landfester, K.; Spiess, H. W. *Acta Polym.* **1998**, *49*, 451.
(133) De Paul, S. M.; Zwanziger, J. W.; Ulrich, R.; Wiesner, U.; Spiess, H. W. *J. Am. Chem. Soc.* **1999**, *121*, 5727.
(134) Zumbulyadis, N. *Phys. Rev. B: Condens. Matter* **1986**, *33*, 6495.
(135) Schmidt-Rohr, K.; Clauss, J.; Spiess, H. W. *Macromolecules* **1992**, *25*, 3273.
(136) *Polymer Handbook*, 3rd ed.; John Wiley and Sons: New York, 1989.
(137) Clauss, J.; Schmidt-Rohr, K.; Spiess, H. W. *Acta Polym.* **1993**, *44*, 1.
(138) VanderHart, D. L. *Macromolecules* **1994**, *27*, 2837.
(139) Egger, N.; Schmidt-Rohr, K.; Blümich, B.; Domke, W. D.; Stapp, B. *J. Appl. Polym. Sci.* **1992**, *44*, 289.
(140) Cai, W. Z.; Schmidt-Rohr, K.; Egger, N.; Gerharz, B.; Spiess, H. W. *Polymer* **1993**, *34*, 267.

(141) Melosh, N. A.; Lipic, P.; Bates, F. S.; Wudl, F.; Stucky, G. D.; Fredrickson, G. H.; Chmelka, B. F. *Macromolecules* **1999**, *32*, 4332.
(142) Ulrich, R. *Morphologien und Eigenschaften strukturierter organisch-anorganischer Hybridmaterialien*; Logos-Verlag: Berlin, 2000.
(143) Huse, D. A.; Leibler, S. *J. Phys. (Paris)* **1988**, *49*, 605.
(144) Finnefrock, A. C.; Ulrich, R.; Du Chesne, A.; Honeker, C. C.; Schumacher, K.; Gruner, S. M.; Wiesner, U.; Unger, K. K. *Angew. Chem., Int. Ed.* **2001**, *40*, 1207.
(145) Pochan, D. J.; Gido, S. P.; Pispas, S.; Mays, J. W.; Ryan, A. J.; Fairclough, J. P. A.; Hamley, I. W.; Terrill, N. J. *Macromolecules* **1996**, *29*, 5091.
(146) Kinning, D. J.; Winey, K. I.; Thomas, E. L. *Macromolecules* **1988**, *21*, 3502.
(147) Majnusz, J.; Catala, J. M.; Lenz, R. W. *Eur. Polym. J.* **1983**, *19*, 1043.
(148) Ballauff, M. *Angew. Chem., Int. Ed. Engl.* **1989**, *28*, 253.
(149) Wegner, G. *Mol. Cryst. Liq. Cryst.* **1993**, *235*, 1.
(150) Bassett, D. R.; Hoy, K. L. *ACS Symp. Ser.* **1981**, *165*, 371.
(151) Geck, M.; Deubzer, B.; Weis, J. *Angew. Makromol. Chem.* **1994**, *223*, 203.
(152) Giannelis, E. P. *Adv. Mater.* **1996**, *8*, 29.
(153) Yano, K.; Usuki, A.; Okada, A.; Kurauchi, T.; Kamigaito, O. *J. Polym. Sci., Part A: Polym. Chem.* **1993**, *31*, 2493.
(154) Bill, J.; Aldinger, F. *Adv. Mater.* **1995**, *7*, 775.
(155) Avnir, D.; Kaufman, V. R.; Reisfeld, R. *J. Non-Cryst. Solids* **1985**, *74*, 395.
(156) Reisfeld, R. *J. Non-Cryst. Solids* **1990**, *121*, 254.
(157) Innocenzi, P.; Kozuka, H.; Yoko, T. *J. Phys. Chem. B* **1997**, *101*, 2285.
(158) Dvorak, O.; DeArmond, M. K. *J. Phys. Chem.* **1993**, *97*, 2646.
(159) Kiernan, P.; McDonagh, C.; MacCraith, B. D.; Mongey, K. *J. Sol-Gel Sci. Technol.* **1994**, *2*, 513.
(160) Castellano, F. N.; Heimer, T. A.; Tandhasetti, M. T.; Meyer, G. J. *Chem. Mater.* **1994**, *6*, 1041.
(161) Matsui, K.; Sasaki, K.; Takahashi, N. *Langmuir* **1991**, *7*, 2866.
(162) MacCraith, B. D.; McDonagh, C. M.; O'Keeffe, G.; Keyes, E. T.; Vos, J. G.; O'Kelly, B.; McGilp, J. F. *Analyst* **1993**, *118*, 385.
(163) McBain, J. W. *The sorption of gases and vapours by solids*; G. Routledge & Sons Ltd.: London, 1932.
(164) Venuto, P. B. *Microporous Mater.* **1994**, *2*, 297.
(165) Gies, H.; Marler, B. *Zeolites* **1992**, *12*, 42.
(166) Huo, Q.; Margolese, D. I.; Ciesla, U.; Demuth, D. G.; Feng, P.; Gier, T. E.; Sieger, P.; Firouzi, A.; Chmelka, B. F.; Schüth, F.; Stucky, G. D. *Chem. Mater.* **1994**, *6*, 1176.
(167) Schumacher, K.; Du Fresne von Hohenesche, C.; Unger, K. K.; Ulrich, R.; Du Chesne, A.; Wiesner, U.; Spiess, H. W. *Adv. Mater.* **1999**, *11*, 1194.
(168) Schumacher, K.; Ravikovitch, P. I.; Du Chesne, A.; Neimark, A. V.; Unger, K. K. *Langmuir* **2000**, *16*, 4648.
(169) Sayari, A. *J. Am. Chem. Soc.* **2000**, *122*, 6504.
(170) Lui, Z.; Sakamoto, Y.; Ohsuna, T.; Hiraga, K.; Terasaki, O.; Ko, C. H.; Shin, H. J.; Ryoo, R. *Angew. Chem., Int. Ed.* **2000**, *39*, 3107.
(171) Grün, M.; Lauer, I.; Unger, K. K. *Adv. Mater.* **1997**, *9*, 254.
(172) Zhao, D.; Feng, J.; Huo, Q.; Melosh, N.; Frederickson, G. H.; Chmelka, B. F.; Stucky, G. D. *Science* **1998**, *279*, 548.
(173) Ying, J. Y.; Mehnert, C. P.; Wong, M. S. *Angew. Chem., Int. Ed.* **1999**, *38*, 56.
(174) Göltner, C. G.; Henke, S.; Weissenberger, M. C.; Antonietti, M. *Angew. Chem., Int. Ed.* **1998**, *37*, 613.
(175) Zhao, D. Y.; Yang, P. D.; Melosh, N.; Feng, Y. L.; Chmelka, B. F.; Stucky, G. D. *Adv. Mater.* **1998**, *10*, 1380.
(176) Yang, P.; Zhao, D.; Margolese, D. I.; Chmelka, B. F.; Stucky, G. D. *Nature* **1998**, *396*, 152.
(177) Yang, P.; Zhao, D.; Margolese, D. I.; Chmelka, B. F.; Stucky, G. D. *Chem. Mater.* **1999**, *11*, 2813.
(178) Brunauer, S.; Deming, L. S.; Deming, W. S.; Teller, E. *J. Am. Chem. Soc.* **1940**, *62*, 1723.
(179) Barrett, E. P.; Joyner, L. G.; Halenda, P. P. *J. Am. Chem. Soc.* **1951**, *73*, 373.
(180) Gregg, S. J.; Sing, K. W. S. *Adsorption, surface area, and porosity*, 2nd ed.; Academic Press: London, 1982.
(181) Ulrich, R.; Garcia, C. B.; Mahajan, S.; Simon, P. F. W.; Zhang, Y.; Wiesner, U. *Polym. Mater. Sci. Eng.* **2001**, *84* (1), 90.
(182) Stadler, R.; Auschra, C.; Beckmann, J.; Krappe, U.; Voigt-Martin, I.; Leibler, L. *Macromolecules* **1995**, *28*, 3080.
(183) Zheng, W.; Wang, Z. *Macromolecules* **1995**, *28*, 7215.
(184) Breiner, U.; Krappe, U.; Abetz, V.; Stadler, R. *Macromol. Chem. Phys.* **1997**, *198*, 1051.
(185) Breiner, U.; Krappe, U.; Thomas, E. L.; Stadler, R. *Macromolecules* **1998**, *31*, 135.
(186) Abetz, V.; Goldacker, T. *Macromol. Rapid Commun.* **2000**, *21*, 16.
(187) Goldacker, T.; Abetz, V. *Macromol. Rapid Commun.* **1999**, *20*, 415.

CM0110674